

EVIDENCE FOR A ROTATIONAL COMPONENT IN THE CGM OF NEARBY GALAXIES*

DAVID M. FRENCH^{1,2} AND BART P. WAKKER²

¹*Space Telescope Science Institute, 3700 San Martin Drive, Baltimore, MD 21218*

²*Department of Astronomy, University of Wisconsin, Madison, WI 53706, USA*

ABSTRACT

We present results of a study comparing the line-of-sight velocity of Ly α absorbers relative to the rotation velocity of nearby galaxy disks in the local Universe ($z \leq 0.03$). We have obtained rotation curves via long-slit spectroscopy of 12 galaxies with the Southern African Large Telescope, and combine this dataset with an additional 17 galaxies with published rotation curves from the literature. Each galaxy appears within $3R_{\text{vir}}$ of a QSO sightline with available Cosmic Origin Spectrograph (COS) data covering the relevant Ly α wavelength range. We present simple cylindrical and NFW galaxy halo rotation models to interpret these data in the context of probing three-dimensional galaxy halos via 1-dimensional QSO absorption-line spectroscopy. Relative to this model we find that up to 63% of Ly α absorbers have velocities consistent with co-rotation. Intriguingly, we find the Ly α co-rotation fraction to decrease with galaxy luminosity (L^*) in a model independent fashion. Finally, we report that both anti-rotating absorbers and those found near luminous galaxies ($L \gtrsim 0.6L^*$) mostly have low Doppler b -parameters ($b \lesssim 50 \text{ km s}^{-1}$). Absorbers consistent with co-rotation show a wide range of Doppler b -parameters. These results are broadly in agreement with the co-rotation fractions predicted by the Stewart et al. (2011b) simulations, and furthermore provide some of the first observational evidence of the cold- and hot-mode accretion regimes predicted to occur in the low- z Universe.

Keywords: galaxies:intergalactic medium, galaxies:evolution, galaxies:halos, quasars: absorption lines

1. INTRODUCTION

Our current Lambda Cold-Dark-Matter (Λ CDM) cosmology picture describes galaxies forming hierarchically out of overdensities in the underlying dark matter distribution. As the surrounding intergalactic medium (IGM) is funneled toward a growing galaxy, simulations predict the angular momentum of the inflowing gas is redistributed onto the disk and seeds the overall rotation of the galaxy (e.g., Stewart et al. 2011a; Chen et al. 2003; Sharma & Steinmetz 2005; Brook et al. 2011; Kimm et al. 2011; Pichon et al. 2011; Stewart et al. 2013). As this infalling gas is responsible for birthing and continuing to feed the galaxies throughout their lifetimes, it is expected that the extended gaseous halos should rotate in the same sense as both the galactic disks and dark matter halos.

In this Λ CDM picture, accretion falls broadly into two types. In the so-called “hot-mode”, gas shock-heats at the virial radius as it encounters the galaxy halo. The inner, more dense region of this hot gaseous halo then rains down onto the disk as it radiatively cools (e.g., Fillmore & Goldreich 1984; Bertschinger 1985; Danovich et al. 2012; Shen et al. 2013). However, most gas arrives cold ($T \sim 10^4 \text{ K}$) from the IGM, and the proposed

radiative shock is unstable to cooling. Thus this hot-halo scenario may not actually be created (Birnboim & Dekel 2003; Kereš et al. 2005; Ocvirk et al. 2008; Brooks et al. 2009; Dekel et al. 2009).

In contrast, as part of the alternative “cold-mode” accretion model, filaments of gas from the IGM would merge smoothly with the disk, thus converting a significant fraction of their infall velocity to rotational velocity of the galaxy (Kereš et al. 2005; Stewart et al. 2017). The simulations of Powell et al. (2011) agreed with these conjectures by showing that indeed, the accreting filaments connect rather smoothly to the disc, even in the presence of strong supernova driven winds. This cold-mode of accretion likely dominates the global growth of all but the most massive halos at high redshifts ($z \gtrsim 3$), and the growth of lower mass ($M_{\text{halo}} \leq 5 \times 10^{11} M_*$) objects at late times (Dekel & Birnboim 2006; van de Voort et al. 2011). Furthermore, cosmological SPH simulations such as those by Stewart et al. (2011b, 2013) suggests that halo gas should co-rotate with disk-gas out to at least 100 kpc, and that absorption in intervening QSO sightlines should be able to accurately capture this rotation signature.

Some observational evidence of cold-mode accretion has been obtained at higher redshifts. In pioneering studies focusing on the Mg II absorber kinematics and their connection with neighboring galaxies, Charlton & Churchill (1998) and Steidel et al. (2002) (and later

* Based on observations made with the Southern African Large Telescope (SALT).

Table 1. SALT Galaxy Observations

Galaxy	R.A.	Dec.	v_{sys}	Published v_{sys}	Type	v_{obs}	$v_{\text{rot}} = v_{\text{obs}} / \sin(i)$	Obs. Date	T_{exp}
			(km s $^{-1}$)	(km s $^{-1}$)		(km s $^{-1}$)	(km s $^{-1}$)		(ks)
(1)	(2)	(3)	(4)	(5)	(6)	(7)	(8)	(9)	(10)
CGCG039-137	11 21 27.0	+03 26 41.7	6918 ± 24	6902 ± 52^a	Scd	132 ± 16	143 ± 25	05 11 2016	700
ESO343-G014	21 37 45.2	-38 29 33.2	9139 ± 32	9162 ± 45^b	S	203 ± 32	203 ± 32	05 16 2016	1000
IC5325	23 28 43.4	-41 20 00.5	1512 ± 8	1503 ± 7^c	SAB(rs)bc	53 ± 5	125 ± 27	05 17 2016	600
MCG-03-58-009	22 53 40.9	-17 28 44.0	9015 ± 19	9030 ± 10^d	Sc	150 ± 11	171 ± 22	05 16 2016	1200
NGC1566	04 20 00.4	-54 56 16.1	1502 ± 15	1504 ± 2^e	SAB(rs)bc	64 ± 8	195 ± 47	10 18 2016	400
NGC3513	11 03 46.1	-23 14 43.8	1204 ± 12	1194 ± 7^c	SB(s)c	11 ± 8	22 ± 24	05 26 2016	600
NGC3633	11 20 26.2	+03 35 08.2	2587 ± 7	2600 ± 2^f	SAa	149 ± 6	157 ± 9	05 11 2016	1200
NGC4536	12 34 27.1	+02 11 17.3	1867 ± 33	1808 ± 1^g	SAB(rc)bc	129 ± 21	148 ± 39	05 11 2016	1300
NGC4939	13 04 14.4	-10 20 22.6	3093 ± 33	3110 ± 4^e	SA(s)bc	204 ± 23	234 ± 39	05 14 2016	500
NGC5364	13 56 12.0	+05 00 52.1	1238 ± 17	1241 ± 4^c	SA(rs)bc pec	130 ± 12	155 ± 23	05 11 2016	700
NGC5786	14 58 56.3	-42 00 48.1	2975 ± 22	2998 ± 5^h	SAB(s)bc	156 ± 14	172 ± 25	05 11 2016	250
UGC09760	15 12 02.4	+01 41 55.5	2094 ± 16	2023 ± 2^i	Sd	46 ± 10	46 ± 16	05 11 2016	500

NOTE—SALT targeted galaxies. Columns are as follows: 1) the galaxy name, 2), 3) R.A., Dec. in J2000, 4) measured galaxy systemic velocity, 5) published galaxy systemic velocity, 6) morphological type (RC3), 7) approaching side velocity, 8) receding side velocity, 9) observation date, and 10) exposure time. All observations used the RSS PG2300 grating.

References—a. Abazajian et al. (2005); b. Jones et al. (2009); c. Corwin et al. (1994); d. Mathewson & Ford (1996); e. Koribalski et al. (2004); f. Lu et al. (1993); g. Grogan et al. (1998); h. di Nella et al. (1996); i. Giovanelli et al. (1997)

Kacprzak et al. 2010; Ho et al. 2017) found tantalizing evidence that a significant fraction of Mg II absorbers have velocities that can be explained by an extended gaseous disk. Additionally, Diamond-Stanic et al. (2016) detect co-rotating H α emission and Mg II and Fe II absorption toward a Milky Way-like galaxy at $z = 0.413$. However, as noted by Steidel et al. (2002), a simple extended disk model is insufficient to explain the observed bulk motion implied by their sample of 5 Mg II absorber-galaxy systems, and a rotating *halo* may be a better model.

Additionally, the picture may have changed since $z \sim 0.5$, the epoch 5 Gyr ago that most of these Mg II systems are probing. By $z \sim 0$ simulations (e.g., Kereš et al. 2005; Stewart et al. 2017) predict a drop-off in cold-mode accretion and a decrease in the density of IGM filaments. Observational confirmation has been even more inconclusive in this low-redshift regime. In the largest such study, involving Ly α absorber-galaxy kinematics, Côté et al. (2005) probed the halos of nine galaxies using *HST* observed background QSOs, and found that large warps would be needed to explain the velocity of H I absorbers by an extended rotating disk. Additionally, Wakker & Savage (2009) compiled a sample of 76 sightlines, which included only 4 galaxy-QSO systems for which the galaxy’s rotation curve was known from the literature, and found only 1/4 of Ly α absorbers appeared to co-rotate with the associated galaxy disk. Similarly, Kacprzak et al. (2011) claim a reduction in Mg II co-rotation around $\sim L^*$ galaxies between $z \sim 0.5$ and $z \sim 0.1$. Approaching the question from a different angle, Bowen et al. (2016) probed the halo of a single galaxy,

NGC1097, with 4 nearby QSO sightlines, and suggests that an extended, slowly rotating disk with additional inflowing IGM material best matches observations.

This current work aims to address many of these observational challenges. Firstly, by significantly increasing the sample size of galaxy-absorber systems, and secondly, by implementing a 3-dimensional rotating halo model to aid in the interpretation challenge inherent in a 1D sightline probing a 3D structure. To significantly improve observational statistics in this low-redshift regime, we have obtained rotation curves from the Southern African Large Telescope (SALT) for 12 nearby spiral galaxies which are located within $3R_{\text{vir}}$ of a background QSO observed by the Cosmic Origins Spectrograph (COS) on *HST*. A literature search yielded an additional 17 galaxies with published rotation curves and known orientations. Each of these is probed by at least one QSO within $3R_{\text{vir}}$.

In Section 2 we describe the selection and reduction of both SALT and COS spectra. In Section 3 we present the rotating halo model we have developed to aid in the interpretation of our observations. In Section 4 we discuss the overall results of this exercise and present a physically-motivated interpretation of these results. See Section 5 for a summary of our results and conclusions. Each galaxy-QSO system is discussed in detail in Appendix A (SALT-observed galaxies) and B (galaxies from the literature).

2. DATA AND ANALYSIS

2.1. SALT Data

Table 2. Summary of QSO Sample

Target (1)	Galaxy (2)	R.A. (3)	Dec. (4)	z (5)	Program (6)	^a T_{exp} (ks) (7)
1H0419-577	NGC1566	04 26 00.7	-57 12 02.0	0.10400	11686	20429
2E1530+1511	NGC5951	15 33 14.3	+15 01 03.0	0.09000	14071	9348
3C232	NGC3067	09 58 20.9	+32 24 02.0	0.53060	8596	44662
3C273.0	NGC4536	12 29 06.7	+02 03 09.0	0.15834	12038	4002
CSO295	NGC3432	10 52 05.6	+36 40 40.0	0.60900	14772	1088
CSO1208	NGC3726	11 40 47.9	+46 22 05.0	0.11500	14729	3052
FBQSJ0908+3246	NGC2770	09 08 38.8	+32 46 20.0	0.25989	14240	7430
H1101-232	NGC3513	11 03 37.7	-23 29 31.0	0.18600	12025	13341
HE0429-5343	NGC1566	04 30 40.0	-53 36 56.0	0.04001	12275	2067
HE1228+0131	NGC4536	12 30 50.0	+01 15 23.0	0.11700	11686	11036
MRC2251-178	MCG-03-58-009	22 54 05.9	-17 34 55.0	0.06609	12029	5515
MRK335	NGC7817	00 06 19.5	+20 12 11.0	0.02578	11524	5122
MRK771	NGC4529	12 32 03.6	+20 09 30.0	0.06301	12569	1868
MRK876	NGC6140	16 13 57.2	+65 43 11.0	0.12900	11524	12579
PG0804+761	UGC04238	08 10 58.7	+76 02 43.0	0.10200	11686	5510
PG1259+593	UGC08146	13 01 12.9	+59 02 07.0	0.47780	11541	9200
PG1302-102	NGC4939	13 05 33.0	-10 33 19.0	0.27840	12038	5979
QSO1500-4140	NGC5786	15 03 34.0	-41 52 23.0	0.33500	11659	9258
RBS1503	NGC5907	15 29 07.5	+56 16 07.0	0.09900	12276	1964
RBS1768	ESO343-G014	21 38 49.9	-38 28 40.0	0.18299	12936	6962
RBS2000	IC5325	23 24 44.7	-40 40 49.0	0.17359	13448	5046
RX_J1017.5+4702	NGC3198	10 17 31.0	+47 02 25.0	0.33544	13314	8655
RX_J1054.2+3511	NGC3432	10 54 16.2	+35 11 24.0	0.20300	14772	533
RX_J1117.6+5301	NGC3631	11 17 40.5	+53 01 51.0	0.15871	14240	4943
RX_J1121.2+0326	CGCG039-137, NGC3633	11 21 14.0	+03 25 47.0	0.15200	12248	2695
RX_J1142.7+4625	NGC3726	11 42 41.2	+46 24 36.0	0.11500	14772	2368
RX_J1236.0+2641	NGC4565	12 36 04.0	+26 41 36.0	0.20920	12248	4235
SBS1116+523	NGC3631	11 19 47.9	+52 05 53.0	0.35568	14240	4949
SBS1503+570	NGC5907	15 04 55.6	+56 49 20.0	0.35894	12276	5163
SDSSJ091052.80+333008.0	NGC2770	09 10 52.8	+33 30 08.0	0.11631	14240	7442
SDSSJ091127.30+325337.0	NGC2770	09 11 27.3	+32 53 37.0	0.29038	14240	10028
SDSSJ09514.80+320357.0	NGC3067	09 59 14.8	+32 03 57.0	0.56462	12603	2273
SDSSJ104335.90+115129.0	NGC3351	10 43 35.9	+11 05 29.0	0.79400	14071	4736
SDSSJ111443.70+525834.0	NGC3631	11 14 43.7	+52 58 34.0	0.07921	14240	13440
SDSSJ112439.50+113117.0	NGC3666	11 24 39.4	+11 31 17.0	0.14300	14071	10427
SDSSJ112448.30+531818.0	UGC06446, NGC3631	11 24 48.3	+53 18 19.0	0.53151	14240	7920
SDSSJ135726.27+043541.4	NGC5364	13 57 26.3	+04 35 41.0	1.23453	12264	14148
SDSSJ151237.15+012846.0	UGC09760	15 12 37.2	+01 28 46.0	0.26625	12603	7590
TON1009	NGC2770	09 09 06.2	+32 36 30.0	0.81028	12603	4740
TON1015	NGC2770	09 10 37.0	+33 29 24.0	0.35400	14240	4774

NOTE—

^a T_{exp} gives the total G130M integration time if multiple exposures were taken.

Our sample contains 12 galaxies observed with the Southern African Large Telescope (SALT) Robert Stobie Spectrograph (RSS) in longslit mode (Burgh et al. 2003; Kobulnicky et al. 2003; Buckley et al. 2006; O'Donoghue et al. 2006). These 12 were selected from a larger pool of 48 submitted targets by the SALT observing queue. We chose these 48 possible targets for their proximity to background QSOs whose spectra contained promising Ly α lines. Finally, we only included galaxies with $z \leq 0.33$ ($cz \leq 10,000 \text{ km s}^{-1}$), angular sizes less than $6'$ to enable easy sky subtraction using the outer edges of the slit and thus avoiding additional, off-target exposures, and surface brightnesses sufficient to keep exposure times below $\sim 1300s$. Table 1 summarizes these observations. Data were taken for 2 additional galaxies, NGC3640 and NGC2962, but proved unusable due to issues with spectral identification and low signal-to-noise (respectively).

All SALT galaxy spectra were reduced and extracted using the standard PySALT reduction package (Crawford et al. 2010)¹, which includes procedures to prepare the data, correct for gain, cross-talk, bias, and overscan, and finally mosaic the images from the 3 CCDs. Next, we rectify the images with wavelength solutions found via Ne and Ar arc lamp spectra line identification. Finally, we perform a basic sky subtraction using an off-target portion of the spectrum, and extract 5-10 pixel wide 1-D strips from the reduced 2-D spectrum.

For each resulting 1-D spectrum, we identify the H α emission lines and perform a non-linear least-squares Voigt profile fit using the Python package LMFIT². While normally Gaussian profiles are used for fitting emission lines, we found a Voigt profile resulted in a better fit of the peak velocity (which is the measurement of prime importance for this analysis). The line centroid and 1σ standard errors are returned, and these fits are then shifted to rest-velocity based on the galaxy systemic redshift with heliocentric velocity corrections calculated via the IRAF *rvcorrect* procedure. The final rotation velocity is calculated by then applying the inclination correction, $v_{\text{rot}} = v / \sin(i)$.

Final errors are calculated as a quadrature sum of 1σ fit errors, systemic redshift error, and inclination uncertainty as follows:

$$\begin{aligned} \sigma^2 = & \left(\frac{\partial v_{\text{rot}}}{\partial \lambda_{\text{obs}}} \right)^2 (\Delta \lambda_{\text{obs}})^2 + \\ & \left(\frac{\partial v_{\text{rot}}}{\partial v_{\text{sys}}} \right)^2 (\Delta v_{\text{sys}})^2 + \\ & \left(\frac{\partial v_{\text{rot}}}{\partial i} \right)^2 (\Delta i)^2, \end{aligned} \quad (1)$$

¹ <http://pysalt.salt.ac.za/>

² <http://cars9.uchicago.edu/software/python/lmfit/contents.html>

where $\Delta \lambda_{\text{obs}}$, Δv_{sys} , and Δi are the errors in observed line center, galaxy redshift, and inclination, respectively. We determine the inclination error by calculating the standard deviation of the set of all axis ratio values available in NED for each galaxy. This inclination component tends to dominate the error for low-inclination galaxies.

The final physical scale is calculated using the SALT image scale of 0.1267 arcsec/pixel, multiplied by the 4-pixel spatial binning, and converted to physical units using a redshift-independent distance if available, and a Hubble flow estimate if not. We adopt a Hubble constant of $H_0 = 71 \text{ km s}^{-1} \text{ Mpc}^{-1}$ throughout.

Finally, we calculate our approaching and receding velocities via a weighted mean of the outer 1/2 of each rotation curve, with errors calculated as weighted standard errors in the mean. Our final redshifts are calculated by forcing symmetric rotation, such that the outer 1/2 average velocity for each side matches in magnitude. The upper-left panel of Figure 1 shows an example of this; the black points and error bars are the observed rotation measurements, the dark green lines show the average rotation velocity for the outer 1/2 edge of each rotation curve, and the green shading shows the 1σ error for this average value. See Appendix A for rotation curves and finder charts for each observed galaxy.

2.2. Additional Galaxy Data

We have augmented our observed sample of galaxies with an additional 17 systems from the literature. While rotation curves for many galaxies have been published, a far smaller sample also included the necessary orientation information for our purposes. Of these, only the 17 included here were also relatively isolated and within $3R_{\text{vir}}$ of a background QSO with sufficient spectral coverage and signal-to-noise. The resulting sample come from a variety of sources, and we have endeavored to keep the galaxy properties (e.g., i , v_{sys}) adopted by the original data authors. For a small subset of these we have adopted more modern inclination and/or position angle measurements where appropriate (see Appendix B for details). We used the plot digitization software WebPlotDigitizer³ to extract rotation curve data from figures when necessary. Rotation velocity errors are calculated with Eq. 1 as for the SALT observed sample.

2.3. COS Spectra

The Barbara A. Mikulski Archive for Space Telescopes (MAST) archives yield 19 QSO targets observed by COS which lie within $3R_{\text{vir}}$ of our SALT galaxies. These targets vary widely in signal-to-noise from approximately 5 to 100 due to our choosing them based only on their proximity to galaxies with known rotation. The reduction procedure for these spectra follow those described by Wakker et al. (2015) and French & Wakker (2017). In

³ WebPlotDigitizer; <http://arohatgi.info/WebPlotDigitizer>

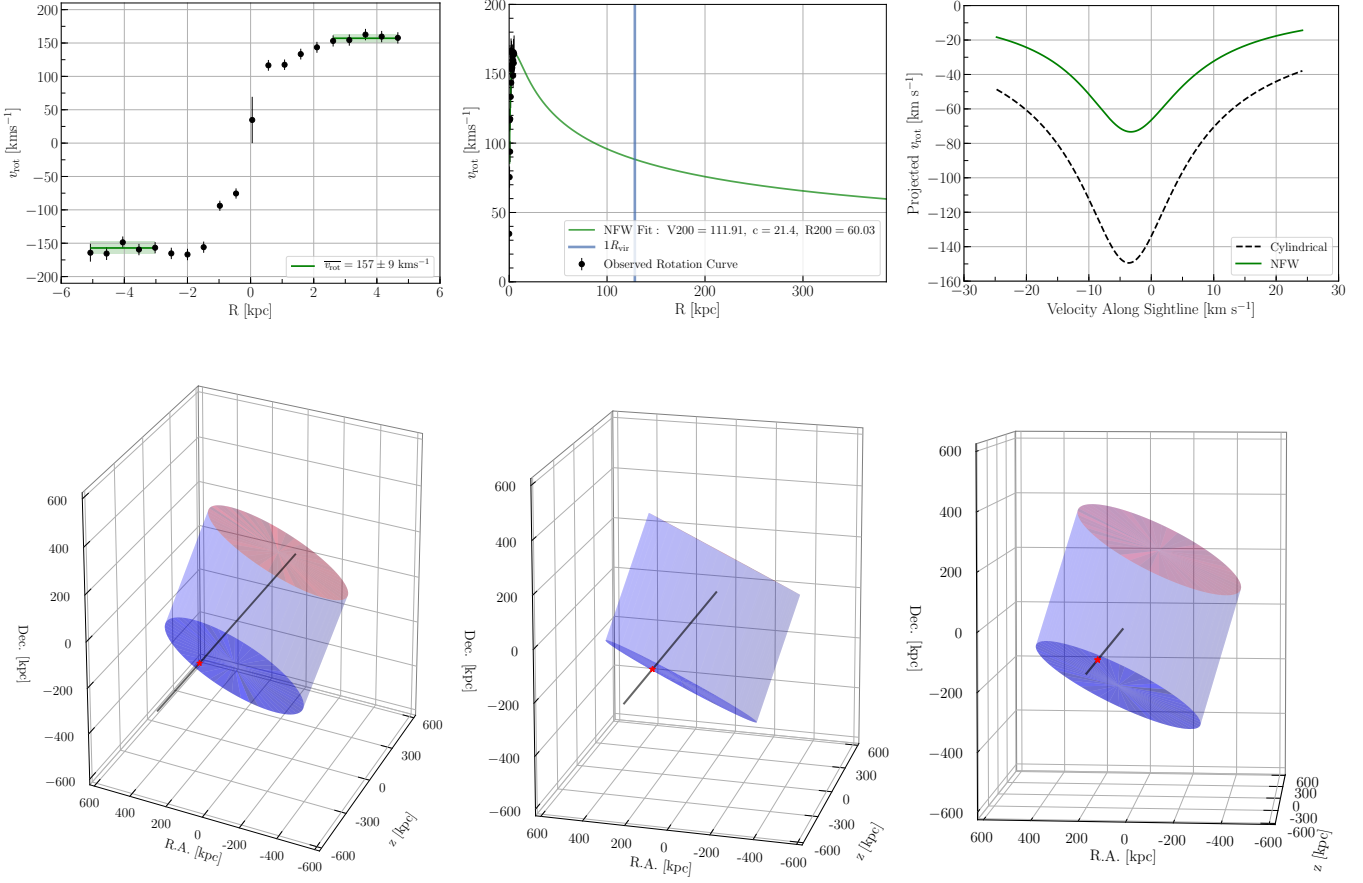


Figure 1. **Top:** Left: The rotation curve for NGC3633 is shown in black, with the outer 1/2 mean rotation velocity indicated in green. Our cylindrical model simply extends this green average velocity out to $3R_{\text{vir}}$. Middle: The observed rotation curve is again shown in black, with an NFW profile fit overlaid in green extending to $3R_{\text{vir}}$ ($1R_{\text{vir}}$ is shown by the vertical blue line). Right: The resulting model velocity predictions for the cylindrical and NFW models are shown in dashed-black and solid-green (respectively). **Bottom:** A 3D example mockup of our halo rotation model showing the orientation and extent of the NGC3633 model from 3 different viewing angles. The approaching extreme edge of the NGC3633 cylindrical halo is shown by dark-blue oval, with the far edge shown in red. The black line shows the location of the sightline toward RX_J1121.2+0326 as it penetrates the halo, with a red star marking the first intercept point.

short, spectra are processed with CALCOS v3.0 or higher and are aligned using a cross-correlation, and then shifted to make sure that (a) the velocities of the interstellar lines match the 21-cm HI profile, and (b) the velocities of lines in a single absorption system line up properly. Multiple exposures are combined by summing total counts per pixel before converting to flux. The COS instrument is described in detail by Green et al. (2012).

Once reduced we make a fourth-order or lower polynomial continuum fit in the region around each absorption line (typically within a 4000 km s^{-1} window around each line) and measure integrated equivalent widths. To recover accurate Doppler b -parameter measurements, we then fit a Voigt profile to each line using the VoigtFit package by Krogager (2018). The VoigtFit routine takes into account instrumental broadening by assuming a

Gaussian with FWHM equal to the instrument spectral resolution (typically 17 km s^{-1} for these COS spectra).

3. HALO ROTATION MODEL

In order to better understand how the 3D rotation of halo gas is mapped onto a 1D QSO sightline, we have developed a simple halo gas rotation model. This model is seeded by an observed rotation curve, which is then extrapolated out to a radius of $3R_{\text{vir}}$ and height of $2R_{\text{vir}}$ to form a coherently rotating halo. For each galaxy-QSO pair we create 2 rotation models: 1) a purely cylindrical halo with constant velocity from the edge of the observed rotation curve out to the edge of our $3 \times 2R_{\text{vir}}$ halo model, and 2) a cylindrical model with rotation velocities which smoothly decline as a function of radius based on a Navarro-Frenk-White (NFW) profile fit (Navarro et al. 1996, 1997).

For the first, purely cylindrical model, the input rotation curve is interpolated via a linear spline fit and extended out to $3R_{vir}$ based on the average velocity of the outer 1/2 radius (see Figure 1; top-left). For the second model, we fit a NFW rotation velocity profile to the input rotation curve. The form of this fit is as follows:

$$V(R) = V_{200} \left[\frac{\ln(1 + cx) - cx/(1 + cx)}{x[\ln(1 + c) - c/(1 + c)]} \right]^{\frac{1}{2}}, \quad (2)$$

where $x = R/R_{200}$, with R_{200} being the radius at which the density contrast with respect to the critical density of the universe exceeds 200, $c = R_{200}/R_s$, with R_s being the characteristic radius of the halo, and V_{200} being the characteristic velocity at R_{200} . We have taken this form from de Blok et al. (2008). The resulting NFW fits tend to be somewhat poor toward the inner parts of the rotation curve (as has been noted by others, e.g., Côté et al. 2005). Regardless, we are most interested in achieving a physically-motivated, declining velocity profile in the outer halo regions where most of our QSO sightlines are located, for which these fits are certainly adequate.

Next, we project the interpolated rotation curve and NFW fit onto a plane oriented to a mock QSO sightline identically to the input galaxy-QSO pair orientation. By then stacking multiple such rotation-planes along the galaxy z-axis direction, we build a simple cylindrical halo model embedded with the fit and interpolated rotation curve. Finally, we calculate the projected rotation velocity encountered at each position along the sightline. The result is a function representing the rotation velocity encountered by the sightline as a function of velocity (i.e., distance) along it. Each model produces the velocity a co-rotating absorber would project onto the spectrum

as a function of velocity along the sightline. Of course, there is an inherent degeneracy between the projected rotation velocity and the velocity along the sightline. For example, a stationary (not co-rotating) absorber located blueward of the galaxy systemic velocity would be indistinguishable from an approaching, co-rotating absorber physically located at the galaxy systemic velocity.

We then collapse this into the range of possible observed velocities by summing the x- and y-velocity ranges generated by each model. This has the effect of combining *both* the projected rotation velocity *and* the physical velocity separation between an absorber and the galaxy's heliocentric velocity ($\Delta v = v_{\text{absorber}} - v_{\text{galaxy}}$) into a single velocity range, which we then can compare to the measured absorption velocity ($v_{\text{Ly}\alpha}$). This resulting velocity range also includes the $1 - \sigma$ rotation curve error estimates as given in the v_{rot} column of Table 3.

Figures 1 illustrates an example model for the SALT-observed galaxy NGC3633, with our observed rotation curve, the NFW fit, and the resulting cylindrical and NFW model output velocity distributions from left-to-right on top, and a 3-D halo mockup from 3 different viewing angles on the bottom. In most cases, and as seen in this example, the two model outputs have similar *shape*, but the NFW profile fit usually results in a lower velocity range (i.e., closer to systemic). Because we combine projected velocity with velocity along the sightline, many models allow for an absorber to have the wrong sign of Δv . For example, an absorber on the approaching side of a halo but at the distant edge would end up with a range of positive Δv consistent with co-rotation because the relatively positive redshift component overcomes the relatively negative rotation component. The result is that some absorbers with the “wrong” on-sky velocity for co-rotation are indeed consistent with co-rotation based on our models.

Table 3. Halo Model Results and Ly α Absorption Properties

#	Galaxy	Target	ρ	Az.	v_{sys}	$v_{\text{rot}}^{\text{a}}$	$v_{\text{Ly}\alpha}$	$W_{\text{Ly}\alpha}$	Cyl. Model ^b	NFW Model ^c
(1)	(2)	(3)	(4)	(5)	(km s $^{-1}$)	(km s $^{-1}$)	(km s $^{-1}$)	(mÅ)	(km s $^{-1}$)	(km s $^{-1}$)
1	CGCG039-137	RX_J1121.2+0326	99	71	6918	143 ± 25	6975	678	6881 - 7079	6881 - 7106
2	ESO343-G014	RBS1768	466	74	9139	-205 ± 32	9308	63	8904 - 9155	8985 - 9176
2	ESO343-G014	RBS1768	466	74	9139	-205 ± 32	9360	306	8904 - 9155	8985 - 9176
2	ESO343-G014	RBS1768	466	74	9139	-205 ± 32	9434	161	8904 - 9155	8985 - 9176
3	IC5325	RBS2000	314	64	1512	-125 ± 27	1598	35	1467 - 1499	1479 - 1520
4	MCG-03-58-009	MRC2251-178	355	71	9015	171 ± 22	9029	62	8985 - 9171	8969 - 9117
5	NGC1566	1H0419-577	303	10	1502	195 ± 47	1075	249	1534 - 1592	1485 - 1547
5	NGC1566	1H0419-577	303	10	1502	195 ± 47	1123	269	1534 - 1592	1485 - 1547
5	NGC1566	1H0419-577	303	10	1502	195 ± 47	1188	240	1534 - 1592	1485 - 1547
5	NGC1566	1H0419-577	303	10	1502	195 ± 47	1264	91	1534 - 1592	1485 - 1547
5	NGC1566	1H0419-577	303	10	1502	195 ± 47	2020	9	1534 - 1592	1485 - 1547

Table 3 continued

Table 3 (*continued*)

#	Galaxy	Target	ρ	Az.	v_{sys}	$v_{\text{rot}}^{\text{a}}$	$v_{\text{Ly}\alpha}$	$W_{\text{Ly}\alpha}$	Cyl. Model ^b	NFW Model ^c
(1)	(2)	(3)	(kpc)	(deg)	(km s $^{-1}$)	(km s $^{-1}$)	(km s $^{-1}$)	(mÅ)	(km s $^{-1}$)	(km s $^{-1}$)
			(4)	(5)	(6)	(7)	(8)	(9)	(10)	(11)
6	NGC1566	HE0429-5343	256	60	1502	-195 \pm 47	1167	79	1439 - 1506	1470 - 1525
6	NGC1566	HE0429-5343	256	60	1502	-195 \pm 47	1358	136	1439 - 1506	1470 - 1525
7	NGC2770	FBQSJ0908+3246	204	59	1948	148 \pm 6	1915	202	1798 - 1946	1825 - 1959
7	NGC2770	FBQSJ0908+3246	204	59	1948	148 \pm 6	1982	230	1798 - 1946	1825 - 1959
8	NGC2770	TON1009	267	41	1948	148 \pm 6	1908	111	1798 - 1912	1832 - 1937
8	NGC2770	TON1009	267	41	1948	148 \pm 6	1980	243	1798 - 1912	1832 - 1937
9	NGC2770	TON1015	218	61	1948	148 \pm 6	1833	244	1949 - 2097	1936 - 2069
9	NGC2770	TON1015	218	61	1948	148 \pm 6	1985	80	1949 - 2097	1936 - 2069
10	NGC2770	SDSSJ091052.80+333008.0	239	66	1948	148 \pm 6	1824	266	1952 - 2097	1939 - 2066
10	NGC2770	SDSSJ091052.80+333008.0	239	66	1948	148 \pm 6	1975	68	1952 - 2097	1939 - 2066
11	NGC2770	SDSSJ091127.30+325337.0	234	30	1948	148 \pm 6	2063	271	1794 - 1909	1825 - 1932
12	NGC3067	3C232	11	74	1465	143 \pm 9	1408	2092	1336 - 1490	1318 - 1491
12	NGC3067	3C232	11	74	1465	143 \pm 9	1510	700	1336 - 1490	1318 - 1491
12	NGC3067	3C232	11	74	1465	143 \pm 9	1641	1635	1336 - 1490	1318 - 1491
13	NGC3067	SDSSJ095914.80+320357.0	128	43	1465	143 \pm 9	1493	623	1472 - 1607	1451 - 1555
14	NGC3198	RX_J1017.5+4702	370	55	660	152 \pm 5	629	71	502 - 641	565 - 668
15	NGC3351	SDSSJ104335.90+115129.0	31	43	778	199 \pm 16	717	823	632 - 797	670 - 804
15	NGC3351	SDSSJ104335.90+115129.0	31	43	778	199 \pm 16	882	621	632 - 797	670 - 804
15	NGC3351	SDSSJ104335.90+115129.0	31	43	778	199 \pm 16	1030	391	632 - 797	670 - 804
16	NGC3432	CSO295	20	82	617	119 \pm 8	600	568	580 - 670	580 - 759
16	NGC3432	CSO295	20	82	616	119 \pm 8	662	585	579 - 669	579 - 758
17	NGC3432	RX_J1054.2+3511	290	57	616	119 \pm 8	703	184	613 - 744	605 - 735
18	NGC3513	H1101-232	60	67	1204	22 \pm 24	1182	635	1182 - 1233	1183 - 1233
19	NGC3631	RX_J1117.6+5301	78	75	1156	143 \pm 25	1131	374	1163 - 1186	1150 - 1178
19	NGC3631	RX_J1117.6+5301	78	75	1156	143 \pm 25	1259	62	1163 - 1186	1150 - 1178
20	NGC3631	SBS1116+523	163	40	1156	143 \pm 25	-99	-99	1094 - 1156	1118 - 1171
21	NGC3631	SDSSJ111443.70+525834.0	145	72	1156	143 \pm 25	1163	232	1160 - 1187	1147 - 1181
22	NGC3631	SDSSJ112448.30+531818.0	86	74	1156	143 \pm 25	1019	71	1129 - 1148	1133 - 1163
22	NGC3631	SDSSJ112448.30+531818.0	86	74	1156	143 \pm 25	1141	165	1129 - 1148	1133 - 1163
23	NGC3633	RX_J1121.2+0326	184	58	2587	-157 \pm 9	2605	180	2425 - 2576	2502 - 2599
24	NGC3666	SDSSJ112439.50+113117.0	58	83	1060	127 \pm 6	1047	345	967 - 1080	914 - 1080
24	NGC3666	SDSSJ112439.50+113117.0	58	83	1060	127 \pm 6	1099	272	967 - 1080	914 - 1080
25	NGC3726	CSO1208	369	88	866	162 \pm 10	731	470	839 - 895	837 - 888
25	NGC3726	CSO1208	369	88	866	162 \pm 10	874	506	839 - 895	837 - 888
26	NGC3726	RX_J1142.7+4625	440	86	866	162 \pm 10	818	375	832 - 854	836 - 861
27	NGC4529	MRK771	159	23	2536	106 \pm 15	2553	240	2416 - 2503	2432 - 2517
28	NGC4536	3C273.0	349	11	1867	148 \pm 39	1580	369	1930 - 2022	1841 - 1926
28	NGC4536	3C273.0	349	11	1867	148 \pm 39	2156	42	1930 - 2022	1841 - 1926
28	NGC4536	3C273.0	349	11	1867	148 \pm 39	2267	27	1930 - 2022	1841 - 1926
29	NGC4536	HE1228+0131	338	51	1867	148 \pm 39	1495	160	1881 - 1935	1856 - 1900
29	NGC4536	HE1228+0131	338	51	1867	148 \pm 39	1571	23	1881 - 1935	1856 - 1900
29	NGC4536	HE1228+0131	338	51	1867	148 \pm 39	1686	321	1881 - 1935	1856 - 1900
29	NGC4536	HE1228+0131	338	51	1867	148 \pm 39	1721	303	1881 - 1935	1856 - 1900
29	NGC4536	HE1228+0131	338	51	1867	148 \pm 39	1854	78	1881 - 1935	1856 - 1900
30	NGC4565	RX_J1236.0+2641	147	41	1230	253 \pm 12	1009	365	1228 - 1495	1199 - 1390
30	NGC4565	RX_J1236.0+2641	147	41	1230	253 \pm 12	1166	305	1228 - 1495	1199 - 1390
30	NGC4565	RX_J1236.0+2641	147	41	1230	253 \pm 12	1254	122	1228 - 1495	1199 - 1390
31	NGC4939	PG1302-102	254	61	3093	-234 \pm 39	3448	72	2845 - 3109	2942 - 3131
32	NGC5364	SDSSJ135726.27+043541.4	165	84	1238	155 \pm 23	967	348	1211 - 1370	1207 - 1324
32	NGC5364	SDSSJ135726.27+043541.4	165	84	1238	155 \pm 23	1124	83	1211 - 1370	1207 - 1324
33	NGC5786	QSO1500-4140	453	1	2975	172 \pm 25	3138	177	3062 - 3157	2975 - 3060
34	NGC5907	SBS1503+570	413	47	667	229 \pm 6	708	301	696 - 903	641 - 774

Table 3 continued

Table 3 (*continued*)

#	Galaxy	Target	ρ	Az.	v_{sys}	$v_{\text{rot}}^{\text{a}}$	$v_{\text{Ly}\alpha}$	$W_{\text{Ly}\alpha}$	Cyl. Model ^b	NFW Model ^c
(1)	(2)	(3)	(kpc)	(deg)	(km s $^{-1}$)	(km s $^{-1}$)	(km s $^{-1}$)	(mÅ)	(km s $^{-1}$)	(km s $^{-1}$)
			(4)	(5)	(6)	(7)	(8)	(9)	(10)	(11)
35	NGC5907	RBS1503	478	63	667	229 \pm 6	-99	-99	432 - 659	565 - 701
36	NGC5951	2E1530+1511	55	85	1780	133 \pm 6	1795	507	1748 - 1902	1748 - 1909
36	NGC5951	2E1530+1511	55	85	1780	133 \pm 6	1953	137	1748 - 1902	1748 - 1909
37	NGC6140	MRK876	113	21	910	138 \pm 5	939	379	952 - 1021	948 - 1023
38	NGC7817	MRK335	343	90	2309	178 \pm 6	1954	216	2283 - 2284	2283 - 2285
38	NGC7817	MRK335	343	90	2309	178 \pm 6	2274	150	2283 - 2284	2283 - 2285
39	UGC04238	PG0804+761	148	59	1544	92 \pm 12	1526	62	1538 - 1642	1532 - 1635
39	UGC04238	PG0804+761	148	59	1544	92 \pm 12	1593	32	1538 - 1642	1532 - 1635
40	UGC06446	SDSSJ112448.30+531818.0	143	22	645	79 \pm 6	664	339	636 - 716	630 - 713
41	UGC08146	PG1259+593	114	50	670	82 \pm 3	646	133	655 - 755	651 - 753
41	UGC08146	PG1259+593	114	50	670	82 \pm 3	683	168	655 - 755	651 - 753
42	UGC09760	SDSSJ151237.15+012846.0	123	90	2094	54 \pm 16	2029	506	2064 - 2124	2064 - 2191

NOTE—

^a Galaxy rotation velocity in the direction of the target in column 3.^b Range of heliocentric velocities consistent with cylindrical co-rotation from the location of the target in column 3.^c Range of heliocentric velocities consistent with NFW halo co-rotation from the location of the target in column 3.

4. DISCUSSION

We present data on 41 galaxy-QSO systems, representing 65 individual Ly α component-galaxy matchups, for which we have galaxy information including kinematics, inclination, size and luminosity. This is the largest sample of its kind to date and provides the best yet opportunity to study the kinematic connection between galaxies and their neutral H I halos.

Table 4 summarizes our galaxy-absorber sample and gives the velocity range predicted by each halo model which would be consistent with co-rotation. Unfortunately our sample contains a large number of high-azimuth targets (i.e., the QSO lies close to the projected galaxy minor axis). These high-azimuth systems are inherently uncertain. For even the most edge-on galaxies, reasonable values for the position angle can vary by at least $\sim 5^\circ$, and this becomes even more uncertain for lower inclination galaxies. Because of this inherent uncertainty in every position angle measurement, we have automatically designated every system with an azimuth of 85° or higher as “uncertain.” We do not include these when calculating co-rotation fractions or otherwise separating systems into co- and anti-rotating subsets.

For the remaining sample we designate each system as co-rotating or anti-rotating firstly based on the on-sky apparent velocity orientation. For example, an absorber with positive Δv which is detected on the receding side of a galaxy is labeled “co-rotating” (recall $\Delta v = v_{\text{absorber}} - v_{\text{galaxy}}$, hence a positive value corresponds to absorption with velocity higher than the galaxy systemic). Next, we compare $v_{\text{Ly}\alpha}$ of each absorber to our cylindrical and NFW profile fit model predictions. For example, let’s

consider NGC5786, with an absorber measured in the spectrum of QSO1500-4140 at $v_{\text{Ly}\alpha} = 3138 \text{ km s}^{-1}$. The cylindrical model gives the range of velocities $3062 - 3157 \text{ km s}^{-1}$, which contains $v_{\text{Ly}\alpha} = 3138 \text{ km s}^{-1}$, and would therefore be marked *co-rotating*. However, the NFW model gives a narrower range, $2975 - 3060 \text{ km s}^{-1}$, which does not contain $v_{\text{Ly}\alpha} = 3138 \text{ km s}^{-1}$ and would thus be marked *anti-rotating*.

Table 3 gives the rotation velocity and associated error for each galaxy in Column (7), with the resulting co-rotation velocity ranges for the cylindrical and NFW models given in Columns (10) and (11). In order to broadly account for velocity uncertainties we have calculated our model ranges to include the 1σ rotation velocity errors. We note that the majority of our “co-rotating” sample fall well within the model ranges, so few would be thrown into uncertainty with a change in errors.

4.1. Co-rotation Fraction

Here we consider in aggregate our sample of Ly α absorbers, and the fraction consistent with co-rotation under various cuts and constraints.

To start we consider the fraction of absorbers which appear to be rotating in the same sense as the nearby galaxy. With no cuts of any kind, we find 52% of absorbers have velocities consistent with co-rotation with the nearby galaxy based on apparent velocity only. Figure 2 presents an map of the locations of each absorber relative to its assumed host galaxy. In this figure we have rotated every system such that the galaxy major axes are horizontal with the approaching side on the left. Blue-diamonds indicate the absorber has the appropriate velocity sign for co-rotation, red-crosses indicate an anti-alignment, grey circles indicate uncertain systems

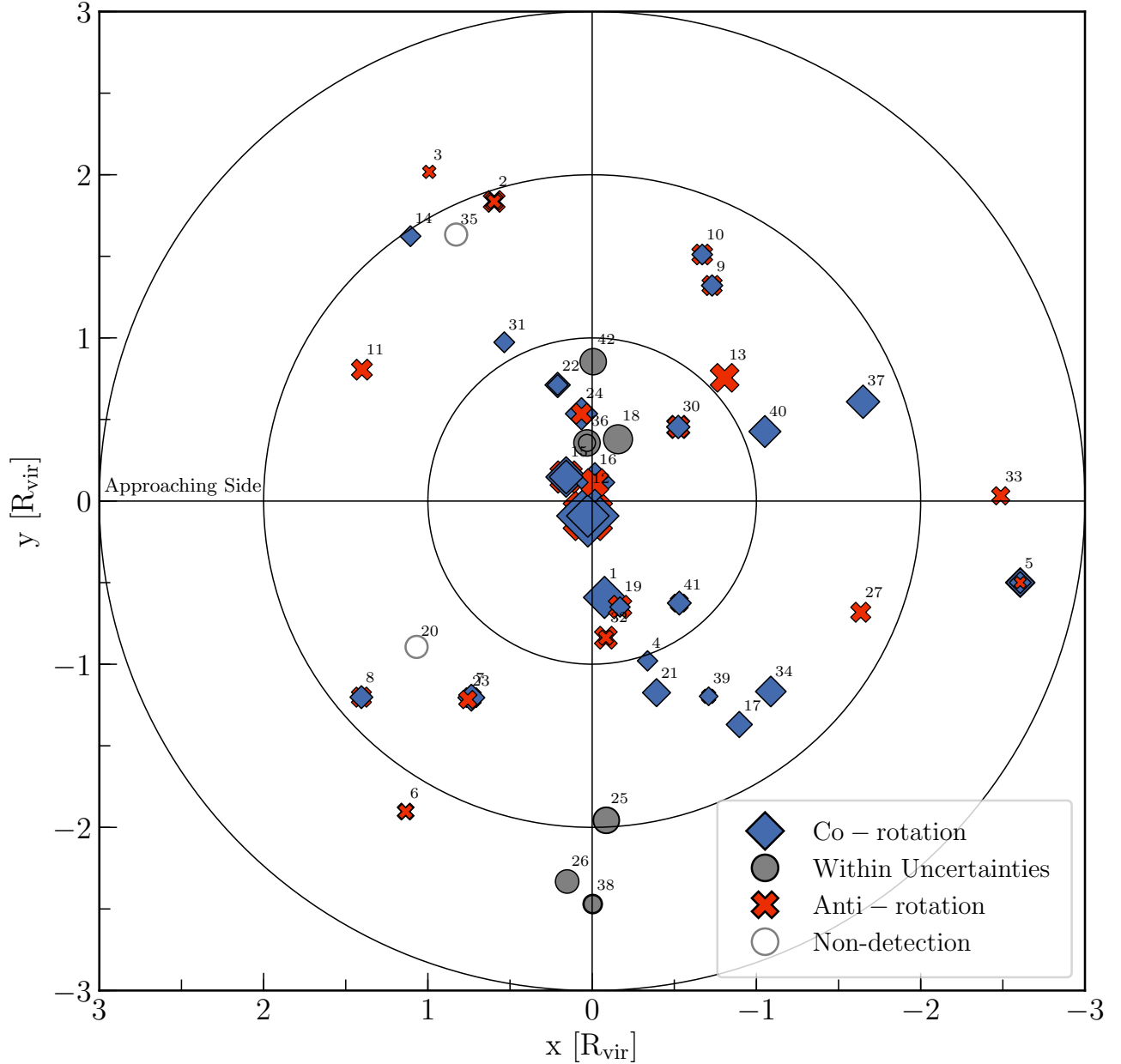


Figure 2. A map of the locations of each absorber normalized with respect to the galaxy virial radius, with *no* additional constraints. The color and style of each point indicates the line-of-sight velocity compared to that of the rotation of the nearby galaxy. Blue diamonds indicate co-rotation, red crosses indicate anti-rotation, and grey circles indicate cases where either is possible due to a combination of orientation and velocity uncertainties. The size of each point is scaled to reflect the EW of the absorber. Concentric rings indicate distances of 1, 2, and $3 R_{\text{vir}}$. All galaxies are rotated to PA = 90° or 270° , such that their major axis' are horizontal and their approaching side is on the left as indicated. The number identifiers correspond to the system number given in column (1) of Table 3.

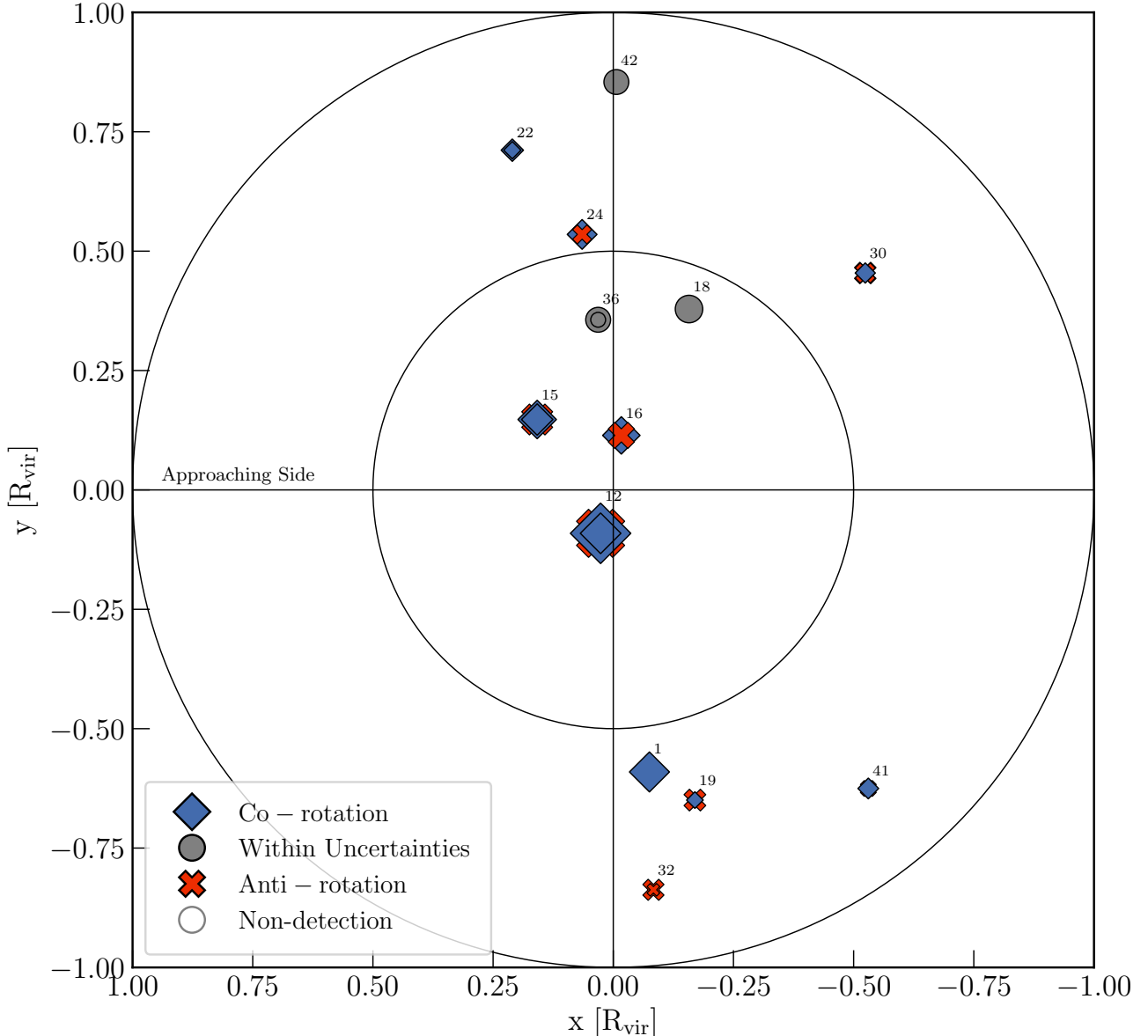


Figure 3. A map of the locations of each absorber normalized with respect to the galaxy virial radius. A zoom in showing only those systems within $1R_{\text{vir}}$ (exactly the same as Figure 2 within $1R_{\text{vir}}$). The color and style of each point indicates the line-of-sight velocity compared to that of the rotation of the nearby galaxy. Blue diamonds indicate co-rotation, red crosses indicate anti-rotation, and grey circles indicate cases where either is possible due to a combination of orientation and velocity uncertainties. The size of each point is scaled to reflect the EW of the absorber. All galaxies are rotated to PA = 90° or 270°, such that their major axis' are horizontal and their approaching side is on the left as indicated. The number identifiers correspond to the system number given in column (1) of Table 3.

due to their high azimuth angles, and open grey circles indicate non-detections. We have also scaled the size of each marker according to it's relative EW, and annotated each with a number corresponding to the appropriate system number given in Column (1) of Table 3. Figure 3 shows the same map zoomed in to a radius of $1R_{\text{vir}}$.

A cursory look at Figures 2 and 3 reveals several interesting results. First, the highest EW absorbers are

all found within $1R_{\text{vir}}$. This is not surprising, given the results by numerous groups claiming an impact parameter - equivalent width anti-correlation (see e.g., French & Wakker 2017, and references therein). Second, many of our absorbers, and many co-rotating ones, lie in the $1 - 2R_{\text{vir}}$ region. Previously, most groups have concentrated on studying the sub- $1R_{\text{vir}}$ regime, but doing so clearly does not reveal the whole physical picture. Third,

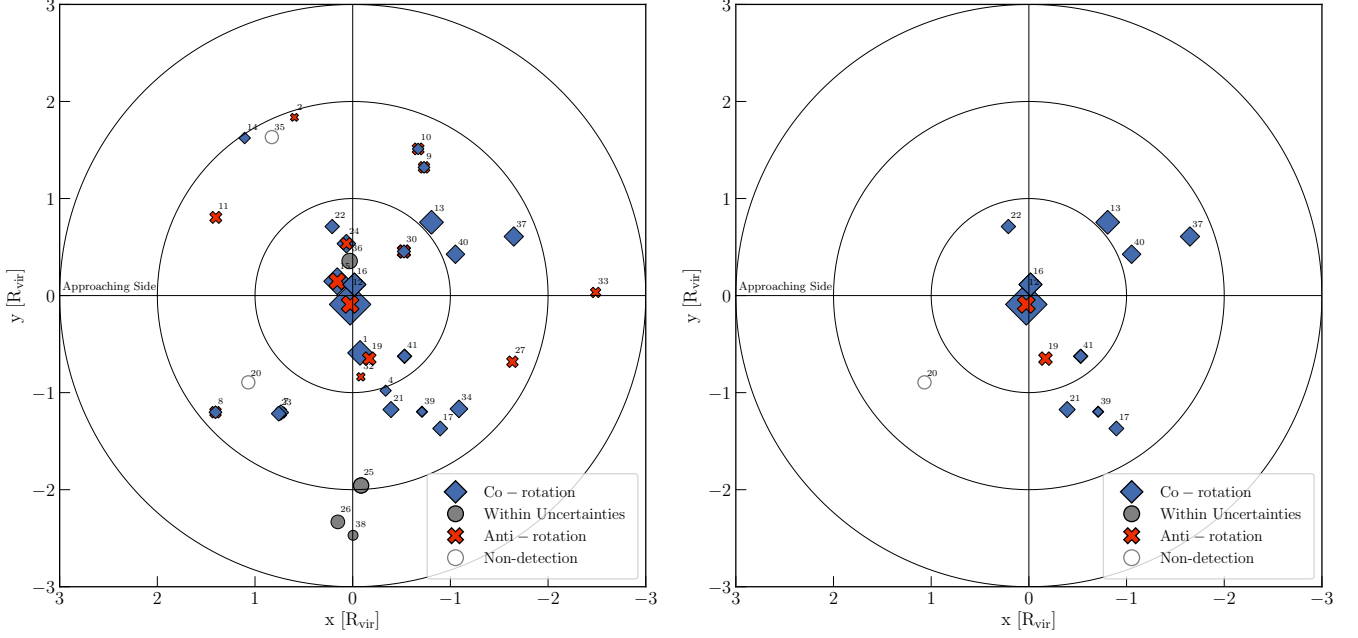


Figure 4. Maps of the locations of each absorber normalized with respect to the galaxy virial radius. The color and style of each point indicates the NFW rotation model results for each absorber with a $v_{\text{Ly}\alpha} \leq v_{\text{rot}}$ constraint imposed. The *right* panel includes only those absorbers near $L^* \leq 0.6$ galaxies. Concentric rings indicate distances of 1, 2, and 3 R_{vir} . Blue diamonds indicate co-rotation, red crosses indicate anti-rotation, and grey circles indicate cases where either is possible due to a combination of orientation and velocity uncertainties. The size of each point is scaled to reflect the EW of the absorber. All galaxies are rotated to PA = 90° or 270°, such that their major axis' are horizontal and their approaching side is on the left as indicated. The number identifiers correspond to the system number given in column (1) of Table 3.

just over half (52%) of galaxy-QSO systems reveal multiple distinct velocity components, and they tend to be oriented such that one component is co- and one anti-rotating with the nearby galaxy.

However, a more in-depth look at the underlying data reveals that many of these absorbers have Δv much larger than the inclination-corrected galaxy rotation velocity (v_{rot}). In other words, the velocity of the absorber relative to galaxy systemic is much greater than the rotation velocity of the galaxy disk. This results in a much smaller fraction of co-rotating absorbers when compared to our cylindrical and NFW profile models (41% and 45%, respectively), which will never output a velocity higher than v_{rot} . In undertaking this study we necessarily must begin by assuming that absorption within some velocity limit and impact parameter from a galaxy is likely associated with that galaxy. To start with we set these limits at $\Delta v_{\text{max}} = 400 \text{ km s}^{-1}$ and $\rho_{\text{max}} = 3R_{\text{vir}}$.

Let us now instead consider only absorbers with $|\Delta v| \leq v_{\text{rot}} \text{ km s}^{-1}$, or absorbers with velocities differences no greater than the maximal galaxy rotation velocity (in other words the we are only considering absorbers where $|v_{\text{Ly}\alpha} - v_{\text{sys}}| \leq v_{\text{rot}} \text{ km s}^{-1}$, which are those absorbers within the velocity range of \pm rotation – this constraint removes 22 from our original sample of 65 absorbers). This constraint thus focuses only on absorbers whose

velocity falls within the range of possible rotation-related velocities. While this could be interpreted as a bias in the sample, we are really only setting the Δv velocity separation limit on a case-by case basis instead of globally given the additional information available to us. We could just as easily have started this study by looking for only absorbers within $\Delta v = 150 \text{ km s}^{-1}$ of a galaxy instead of $\Delta v = 400 \text{ km s}^{-1}$, which would have a similar overall effect. This criteria instead narrows the focus to only those absorbers kinematically close enough to a galaxy to test for a co-rotation fraction with minimal contamination from Ly α forest lines.

With this rotation-based velocity constraint in place the co-rotating fractions for our cylindrical and NFW models increase to 58% and 63%, while the apparent co-rotation fraction decreases slightly to 50%. Consistently, we find our cylindrical model to predict an $\sim 8 - 10\%$ higher co-rotation fraction than the straight apparent velocity analysis yields, and our NFW model tends to predict an additional $\sim 5\%$ increase. This is a not wholly unexpected, and yet refreshing result; simulations have predicted that galaxies are strongly linked to their surroundings and share angular momentum, which should result in a higher than 50% halo-gas co-rotation fraction. However, the simple apparent on-sky velocity method ignores the complexities of sampling a 3-dimensional

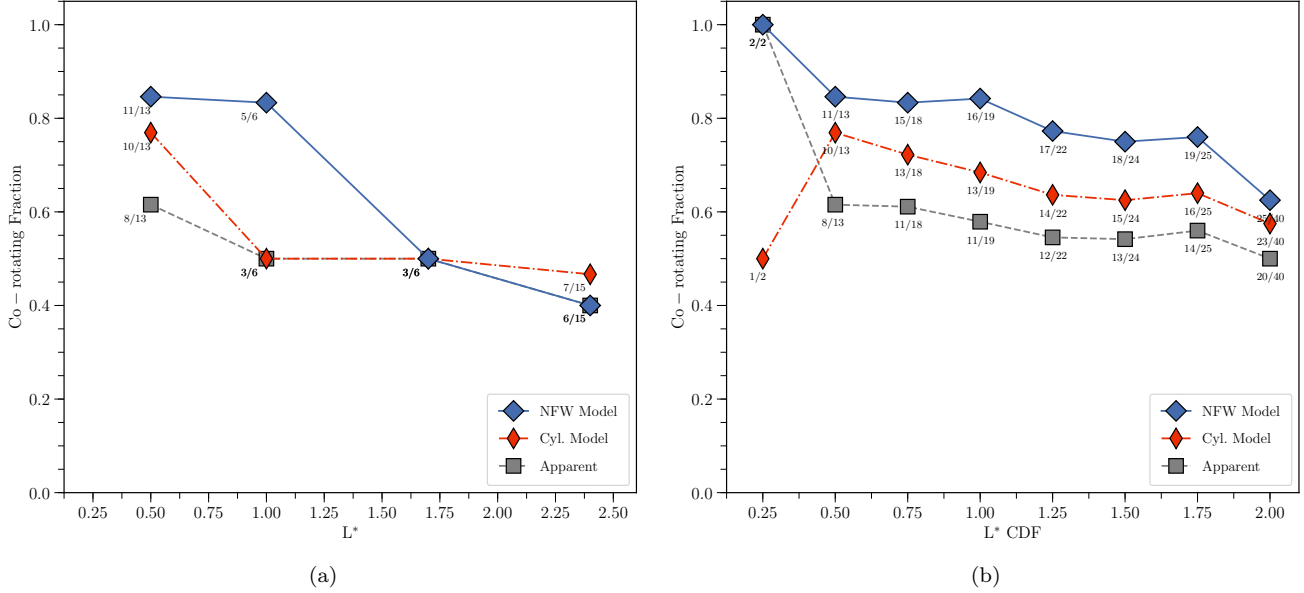


Figure 5. Top: The fraction of co-rotating absorbers as a function of L^* . The upper edges of the L^* bins are located at 0.5, 1.0, 1.7, and $> 1.7 L^*$ (i.e., all systems $1.7L^*$ and higher). **Bottom:** The fraction of co-rotating absorbers as a function of cumulative L^* distribution. All systems are included at the $L^* = 2.0$ bin (this bin includes galaxies brighter than $2.0L^*$ as well), then only galaxies with $L^* \leq 1.8$ are included at $L^* = 1.8$, and so on.

structure with a 1-dimensional QSO sightline. It appears then that the NFW model, the most physically motivated of the three, systematically recovers a higher fraction of this co-rotating gas. For brevity's sake we will concentrate only on the NFW model results from here onwards. Figure 4.1 shows another absorber location map, this time colored according to our NFW model results.

4.2. Co-rotation as a function of L^*

Next, we consider the effect of galaxy luminosity. We separate our sample around $0.6L^*$, while keeping our $|\Delta v| \leq v_{\text{rot}} \text{ km s}^{-1}$ constraint in place. This results in 15 absorbers near $L \leq 0.6L^*$ galaxies and 30 around more luminous galaxies. The co-rotating fraction around luminous galaxies is then 48%, compared to 87% around $L \leq 0.6L^*$ galaxies. Figure 4.1 shows an absorber map for these $L \leq 0.6L^*$ galaxies only.

Furthermore, we find this co-rotation fraction smoothly decreases as a function of L^* , as shown in Figure 5(a). In this figure we have binned galaxy-absorber systems into the following 4 ranges: $L/L^* = [0 - 0.5]$, $(0.5 - 1.0]$, $(1.0 - 1.7]$, and $(1.7 - \infty)$. This uneven bin spacing was chosen to produce as evenly occupied bins as possible, and does not affect the overall trend. Unfortunately there are a large number of systems between $1.7 - 1.8 L^*$, so no splitting exists to produce perfectly even bins. The co-rotation fraction is labeled explicitly underneath each data point for clarity.

In Figure 5(b) we consider the co-rotation fraction as a function of the cumulative L^* distribution (i.e., every

consecutive L^* bin includes all previous bins' data as well). Here, bins are evenly distributed in $0.25L^*$ increments with the final bin containing all systems. Thus, nearly 90% of absorbers near L^* or fainter galaxies are co-rotating based on our NFW model results, but this fraction decreases to $\sim 80\%$ for $1.5L^*$ or fainter galaxies, and to 63% for all galaxies. As seen in Figure 5(b), this trend is also model independent; it appears nearly identically but offset downward in both the cylindrical model (red-rhombus) and apparent velocity only (grey-square) samples.

Given recent simulation results suggesting that co-rotating accretion gas is predominately cold-mode for low-mass galaxies in the local Universe, this may be a signature of this co-rotating, cold-mode accreting gas. Additionally, Lutz et al. (2018) find that galaxies with high H I mass compared to their stellar mass have higher halo angular momentum, which may be impeding their ability to efficiently form stars. While we do not have independent measures of H I and stellar mass for our galaxies, it may not be unreasonable to think that these high angular momentum galaxies reside toward the lower luminosity end of our sample.

4.3. Doppler b -parameters

Finally, we consider the Doppler b -parameters of our absorber sample. Figure 6(a) shows the distribution of b -parameters for all velocity-constrained Ly α absorbers ($|\Delta v| \leq v_{\text{rot}} \text{ km s}^{-1}$). In the top panel of Figure 6(a) we separate them into co-rotating and anti-rotating subsets, in the middle panel we do the same but only for

$\rho \leq 1R_{\text{vir}}$, and on the bottom we separate based on absorbers near $L^* \leq 0.6$ and $L^* > 0.6$ galaxies. Interestingly, we find that *lower* b -parameter absorbers tend to be both anti-rotating and found near $L^* > 0.6$ galaxies. As previously discussed however, the picture described by the simulations of Stewart et al. (2011b) and others describes a scenario where co-rotating gas is predominately the product of cold-mode accretion. Hotter, outflowing gas would likely carry angular momentum from the disk with it, but this would be quickly lost as the outflows expand into the halo and result in negligible observable rotation signature.

In Figure 6(b) we show how the b -parameters vary as a function of Δv for co-rotating versus anti-rotating absorbers. We would expect the co-rotating sample to occupy a narrower Δv space based on their definition (Δv fitting within the velocity bounds given by our NFW model), but the elevated b -parameters for these compared to the relatively flat distribution for anti-rotators is intriguing. Aside from a single Ly α line toward SDSSJ104335.90+115129.0 and NGC3351, all the anti-rotators have $b \lesssim 50 \text{ km s}^{-1}$. As these are higher than expected for purely thermal motions within a single Ly α structure, we may be observing either a number of clouds that are close in velocity space or a filament with a range of turbulent, internal velocities. In this scenario these high b -parameters would be consistent with filamentary inflows versus around higher L^* galaxies where virial shocks are perhaps breaking larger structures into smaller, more isolated clouddlets and producing lower b -parameter absorption.

5. SUMMARY

We have presented complimentary COS Ly α absorption-line and nearby galaxy rotation curve analysis for a sample of 42 galaxy-QSO pairs, resulting in the largest yet sample of its kind. Our main conclusions are the following:

1. The fraction of Ly α absorbers appearing to co-rotate with the nearby galaxy smoothly declines as a function galaxy luminosity (L^*). Our overall co-rotation fraction is consistent with the simulation results of Stewart et al. (2011b, 2013), and effect of galaxy luminosity on halo gas co-rotation is consistent with predicted cold-mode filamentary accretion schemes.

2. Based on the predicted velocity of the NFW halo model, 87% of absorbers co-rotate around $\leq 0.6L^*$ galaxies, which falls to 77% around $\leq 1.5L^*$ galaxies, and down to 63% around all galaxies at $z \sim 0$.

3. Two thirds of all Ly α absorbers are found with velocity separations less than or equal to the nearby galaxy rotation velocity ($\Delta v \leq |v_{\text{rot}}| \text{ km s}^{-1}$). This includes systems with multiple galaxies and undoubtedly complex velocity fields. Restricting this study to only

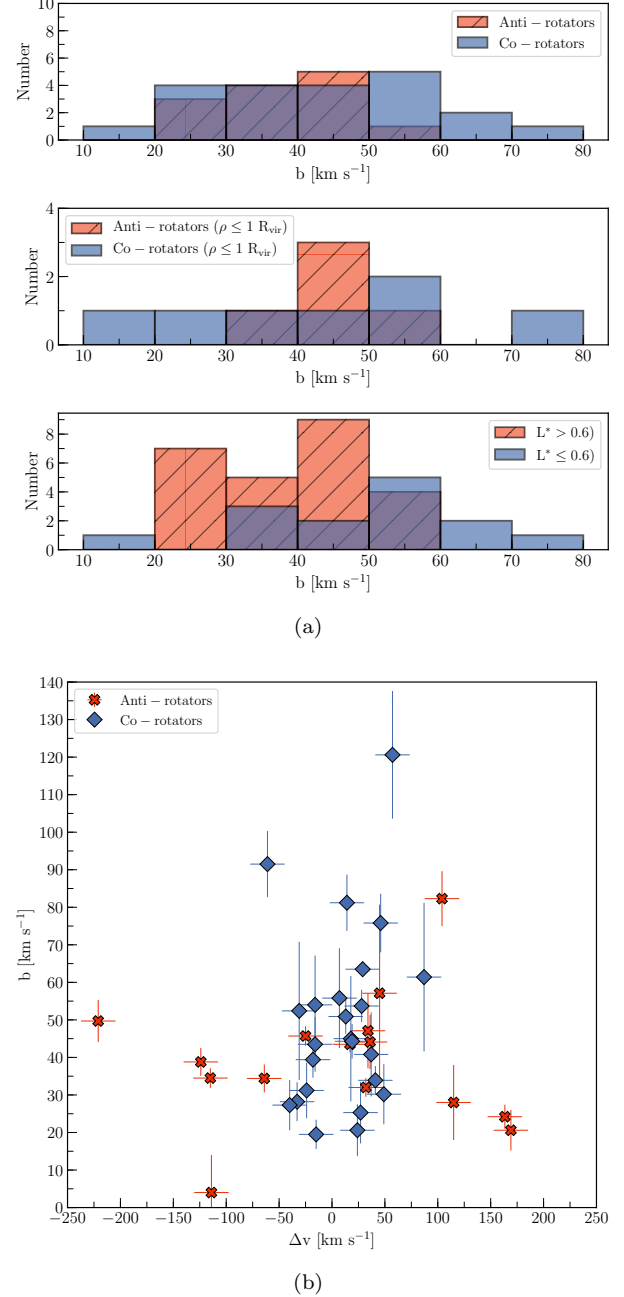


Figure 6. Top: The distributions of Doppler b -parameters for all Ly α absorbers with $\Delta v \leq v_{\text{rot}} \pm 10 \text{ km s}^{-1}$. The co-rotating versus anti-rotating designation here is based on NFW results. In the middle we do the same but only for $\rho \leq 1R_{\text{vir}}$, and on the bottom we separate based on absorbers near $L^* \leq 0.6$ (blue) and $L^* > 0.6$ (red-hatched) galaxies. **Bottom:** The Doppler b -parameters of each absorber as a function of Δv , split into co-rotating (blue diamonds) and anti-rotating (red crosses). The data point for the NGC3067-3C232 LLS ($b = 245.2 \pm 25.9$, $\Delta v = -68.0 \pm 11 \text{ km s}^{-1}$, co-rotating) is not shown in order to highlight the majority distribution in greater detail.

Table 4. CGM Rotation: Summary of Results

Sub-sample	Co-rotating	Anti-rotating	Uncertain	Co-rotating	Anti-rotating	Co-rotating	Anti-rotating
				$\rho \leq 1$	$\rho \leq 1$	$\rho > 1$	$\rho > 1$
Apparent Vel.	29	27	9	12	10	17	17
Cyl. Model	23	33	9	10	12	13	21
NFW Model	25	31	9	10	12	15	19
<hr/>							
NFW w/ Constraint: $ \Delta v \leq v_{\text{rot}} \pm 10 \text{ km s}^{-1}$	25	15	5	10	7	15	8
NFW w/ Constraint: Nearest $\rho \geq 20 \text{ kpc}$	12	14	6	2	4	10	10
NFW w/ Both Constraints	12	9	2	2	2	10	7
<hr/>							
NFW w/ Δv Constraint: $[0 \leq L^* \leq 0.6]$	13	2	0	6	2	7	0
NFW w/ Δv Constraint: $[L^* > 0.6]$	12	13	5	4	5	8	8

isolated galaxy-QSO systems would likely result in an even higher fraction.

4. A simple cylindrical halo model with rotation velocities smoothly declining based on an NFW rotation curve fit results in the highest co-rotation fraction for Ly α absorbers (63%).

5. Co-rotating absorbers (when chosen from the sample restricted to $|\Delta v| \leq v_{\text{rot}} \text{ km s}^{-1}$) occupy a wide range in Doppler b -parameter, while anti-rotators have mostly $b \leq 50 \text{ km s}^{-1}$. A remarkably similar split is found for absorbers near $L \leq 0.6L^*$ vs $L > 0.6L^*$ galaxies. This could add further evidence for our proposed cold-mode accretion explanation if these enhanced b -parameters are caused by the blending of multiple absorption components close in velocity space within a filament.

D. M. F. thanks Claire Murray for useful insights, particularly related to our halo model, and Julie Davis for invaluable SALT data reduction pointers. This research has made use of the NASA/IPAC Extragalactic Database (NED) which is operated by the Jet Propulsion Laboratory, California Institute of Technology, under contract with the National Aeronautics and Space Administration. Based on observations with the NASA/ESA *Hubble Space Telescope*, obtained at the Space Telescope Science Institute (STScI), which is operated by the Association of Universities for Research in Astronomy, Inc., under NASA contract NAS 5-26555. Spectra were retrieved from the Barbara A. Mikulski Archive for Space Telescopes (MAST) at STScI. Some of the observations reported in this paper were obtained with the Southern African Large Telescope (SALT) under program 2016-1-SCI-062 (PI: Wakker). Over the course of this study,

D.M.F. and B.P.W. were supported by grant AST-118913 from the National Science Foundation and GO-14240, GO-14268, and GO-14588 from the Space Telescope Science Institute.

Facility: HST (COS), SALT (RSS)

REFERENCES

- Abazajian, K., Adelman-McCarthy, J. K., Agüeros, M. A., et al. 2005, AJ, 129, 1755
- Bertschinger, E. 1985, ApJS, 58, 39
- Birnboim, Y., & Dekel, A. 2003, MNRAS, 345, 349
- Bowen, D. V., Chelouche, D., Jenkins, E. B., et al. 2016, ApJ, 826, 50
- Brook, C. B., Governato, F., Roškar, R., et al. 2011, MNRAS, 415, 1051
- Brooks, A. M., Governato, F., Quinn, T., Brook, C. B., & Wadsley, J. 2009, ApJ, 694, 396
- Buckley, D. A. H., Swart, G. P., & Meiring, J. G. 2006, in Proc. SPIE, Vol. 6267, Society of Photo-Optical Instrumentation Engineers (SPIE) Conference Series, 62670Z
- Burgh, E. B., Nordsieck, K. H., Kobulnicky, H. A., et al. 2003, in Proc. SPIE, Vol. 4841, Instrument Design and Performance for Optical/Infrared Ground-based Telescopes, ed. M. Iye & A. F. M. Moorwood, 1463–1471
- Carilli, C. L., van Gorkom, J. H., & Stocke, J. T. 1989, Nature, 338, 134
- Charlton, J. C., & Churchill, C. W. 1998, ApJ, 499, 181
- Chen, D. N., Jing, Y. P., & Yoshikawa, K. 2003, ApJ, 597, 35
- Corwin, Jr., H. G., Buta, R. J., & de Vaucouleurs, G. 1994, AJ, 108, 2128
- Côté, S., Wyse, R. F. G., Carignan, C., Freeman, K. C., & Broadhurst, T. 2005, ApJ, 618, 178
- Crawford, S. M., Still, M., Schellart, P., et al. 2010, in Proc. SPIE, Vol. 7737, Observatory Operations: Strategies, Processes, and Systems III, 773725
- Danovich, M., Dekel, A., Hahn, O., & Teyssier, R. 2012, MNRAS, 422, 1732
- de Blok, W. J. G., Walter, F., Brinks, E., et al. 2008, AJ, 136, 2648
- Dekel, A., & Birnboim, Y. 2006, MNRAS, 368, 2
- Dekel, A., Birnboim, Y., Engel, G., et al. 2009, Nature, 457, 451
- di Nella, H., Paturel, G., Walsh, A. J., et al. 1996, A&AS, 118, 311
- Diamond-Stanic, A. M., Coil, A. L., Moustakas, J., et al. 2016, ApJ, 824, 24
- Dicaire, I., Carignan, C., Amram, P., et al. 2008, MNRAS, 385, 553
- Falco, E. E., Kurtz, M. J., Geller, M. J., et al. 1999, PASP, 111, 438
- Fillmore, J. A., & Goldreich, P. 1984, ApJ, 281, 1
- French, D. M., & Wakker, B. P. 2017, ApJ, 837, 138
- Giovanelli, R., Avera, E., & Karachentsev, I. D. 1997, AJ, 114, 122
- Green, J. C., Froning, C. S., Osterman, S., et al. 2012, ApJ, 744, 60
- Grogan, N. A., Geller, M. J., & Huchra, J. P. 1998, ApJS, 119, 277
- Ho, S. H., Martin, C. L., Kacprzak, G. G., & Churchill, C. W. 2017, ApJ, 835, 267
- Jones, D. H., Read, M. A., Saunders, W., et al. 2009, MNRAS, 399, 683
- Kacprzak, G. G., Churchill, C. W., Barton, E. J., & Cooke, J. 2011, ApJ, 733, 105
- Kacprzak, G. G., Churchill, C. W., Ceverino, D., et al. 2010, ApJ, 711, 533
- Keeney, B. A., Momjian, E., Stocke, J. T., Carilli, C. L., & Tumlinson, J. 2005, ApJ, 622, 267
- Kereš, D., Katz, N., Weinberg, D. H., & Davé, R. 2005, MNRAS, 363, 2
- Kimm, T., Slyz, A., Devriendt, J., & Pichon, C. 2011, MNRAS, 413, L51
- Knapen, J. H. 1997, MNRAS, 286, 403
- Kobulnicky, H. A., Nordsieck, K. H., Burgh, E. B., et al. 2003, in Proc. SPIE, Vol. 4841, Instrument Design and Performance for Optical/Infrared Ground-based Telescopes, ed. M. Iye & A. F. M. Moorwood, 1634–1644
- Koribalski, B. S., Staveley-Smith, L., Kilborn, V. A., et al. 2004, AJ, 128, 16
- Krogager, J.-K. 2018, ArXiv e-prints
- Lu, N. Y., Hoffman, G. L., Groff, T., Roos, T., & Lamphier, C. 1993, ApJS, 88, 383
- Lutz, K. A., Kilborn, V. A., Koribalski, B. S., et al. 2018, MNRAS, 476, 3744
- Mathewson, D. S., & Ford, V. L. 1996, ApJS, 107, 97
- Narayanan, A., Wakker, B. P., Savage, B. D., et al. 2010, ApJ, 721, 960
- Navarro, J. F., Frenk, C. S., & White, S. D. M. 1996, ApJ, 462, 563
- . 1997, ApJ, 490, 493
- Ocvirk, P., Pichon, C., & Teyssier, R. 2008, MNRAS, 390, 1326
- O'Donoghue, D., Buckley, D. A. H., Balona, L. A., et al. 2006, MNRAS, 372, 151
- Pichon, C., Pogosyan, D., Kimm, T., et al. 2011, MNRAS, 418, 2493
- Powell, L. C., Slyz, A., & Devriendt, J. 2011, MNRAS, 414, 3671
- Rhee, M.-H., & van Albada, T. S. 1996, A&AS, 115, 407
- Rubin, V. C., Thonnard, N. T., & Ford, Jr., W. K. 1982, AJ, 87, 477
- Sharma, S., & Steinmetz, M. 2005, ApJ, 628, 21
- Shen, S., Madau, P., Guedes, J., et al. 2013, ApJ, 765, 89

- Sofue, Y. 1996, ApJ, 458, 120
- Steidel, C. C., Kollmeier, J. A., Shapley, A. E., et al. 2002, ApJ, 570, 526
- Stewart, K. R., Brooks, A. M., Bullock, J. S., et al. 2013, ApJ, 769, 74
- Stewart, K. R., Kaufmann, T., Bullock, J. S., et al. 2011a, ApJL, 735, L1
- . 2011b, ApJ, 738, 39
- Stewart, K. R., Maller, A. H., Oñorbe, J., et al. 2017, ApJ, 843, 47
- Stocke, J. T., Keeney, B. A., & Danforth, C. W. 2010, PASA, 27, 256
- Swaters, R. A., Sancisi, R., van Albada, T. S., & van der Hulst, J. M. 2009, A&A, 493, 871
- van de Voort, F., Schaye, J., Booth, C. M., Haas, M. R., & Dalla Vecchia, C. 2011, MNRAS, 414, 2458
- Verheijen, M. A. W., & Sancisi, R. 2001, A&A, 370, 765
- Wakker, B. P., Hernandez, A. K., French, D. M., et al. 2015, ApJ, 814, 40
- Wakker, B. P., & Savage, B. D. 2009, ApJS, 182, 378
- Yim, K., Wong, T., Xue, R., et al. 2014, AJ, 148, 127

APPENDIX

A. SALT GALAXIES

In this section we summarize each galaxy-QSO system observed by SALT. We calculate impact parameters to QSOs and galaxy-absorber velocity separations ($\Delta v = v_{\text{Ly}\alpha} - v_{\text{sys}}$) based on our measured v_{sys} values. Both measured and previously published values for v_{sys} are given in Table 1 for reference. We provide rotation curves and finder chart images for the sub-sample of galaxies with newly observed SALT data.

A.1. CGCG039-137

CGCG039-137 is an isolated Scd type galaxy with a measured systemic velocity $v_{\text{sys}} = 6918 \pm 24 \text{ km s}^{-1}$ and inclination of $i = 72^\circ$. The QSO RX_J1121.2+0326 is located nearby at an impact parameter of 99 kpc and azimuth angle of 71° on the receding side. The data for RX_J1121.2+0326 has low signal-to-noise (~ 4.2), but we are able to detect Ly α at 6975 km s^{-1} , which, at $\Delta v = 57 \text{ km s}^{-1}$, lies well within the range of projected velocities consistent with co-rotation (cylindrical model = [-36, 137], NFW = [-37, 164] km s^{-1}).

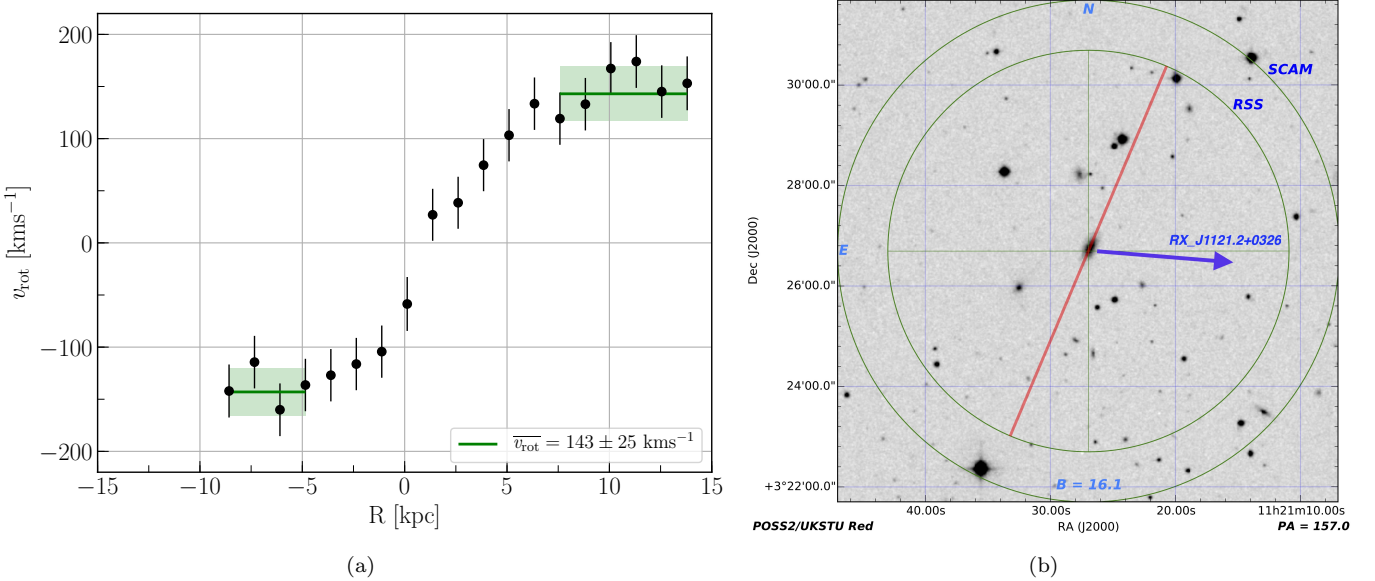


Figure 7. a) Rotation curve of CGCG039-137. The solid green line indicates the weighted mean velocity over the corresponding x-axis region, and the shaded green indicates the 1σ error in the mean. b) SALT finder chart for CGCG039-137 showing the position of the slit in red.

A.2. ESO343-G014

ESO343-G014 is an edge-on ($i = 90^\circ$) spiral galaxy with a measured systemic velocity $v_{\text{sys}} = 9139 \pm 32 \text{ km s}^{-1}$. It has a smaller neighboring galaxy, 2MASXJ21372816-3824412, located north of its major axis at a projected distance of 216 kpc and velocity of 9129 km s^{-1} . The nearest sightline is towards RBS1768 at $\rho = 466$ kpc and 74° azimuth angle on the approaching side. We detect 3 blended Ly α absorption components toward RBS1768 at $v_{\text{Ly}\alpha} = 9308, 9360, 9434 \text{ km s}^{-1}$ ($\Delta v = 169, 221, 295 \text{ km s}^{-1}$). This system is highly blended with galactic S II, and therefore their widths are not reliable. All of these are anti-aligned with the rotation of ESO343-G014 relative to the models (cylindrical = [-203, 10], NFW = [-122, 31] km s^{-1}). Unfortunately the presence of 2MASXJ21372816-3824412 makes it difficult to attribute this gas uniquely to ESO343-G014. Additionally, this gas could be attributed to either the approaching or receding side of the disk due to the large impact parameter and high azimuth angle of the sightline.

A.3. IC5325

IC5325 is a mostly face-on ($i = 25^\circ$) SAB(rs)bc type galaxy with a measured systemic velocity $v_{\text{sys}} = 1512 \pm 8 \text{ km s}^{-1}$. Its inclination is just high enough to obtain a reasonable rotation curve. The closest neighboring galaxy is ESO347-G020 to the southeast at 306 kpc and $v_{\text{sys}} = 1745 \text{ km s}^{-1}$. Three other much smaller galaxies are also

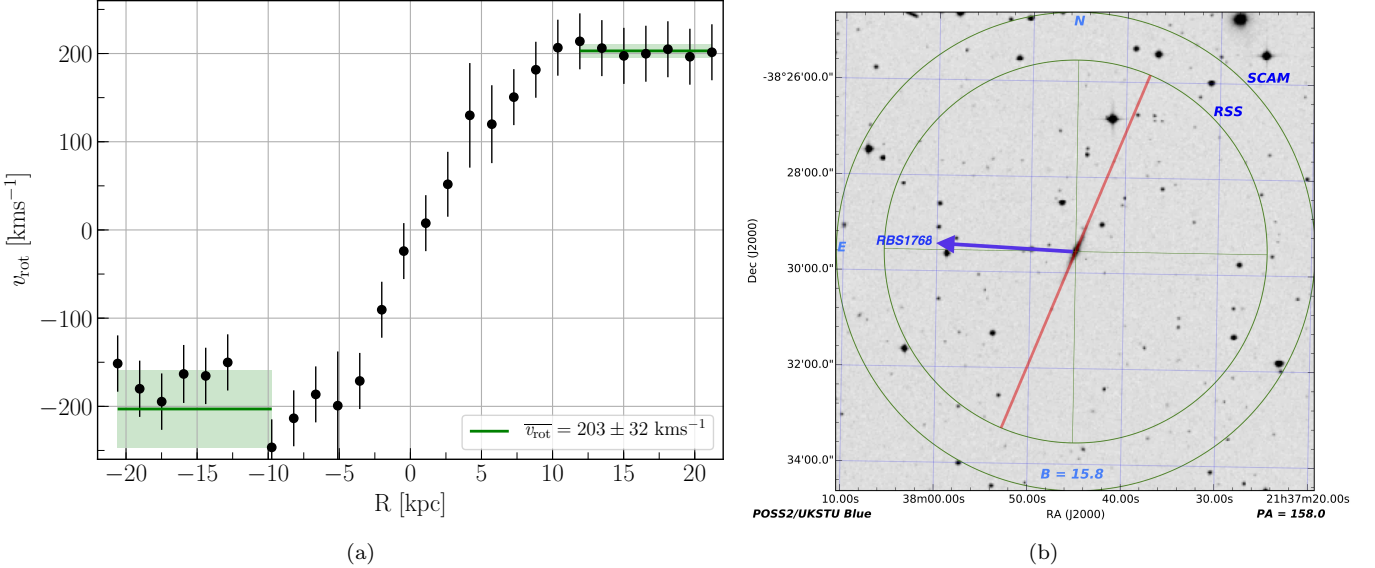


Figure 8. a) Rotation curve of ESO343-G014. The solid green line indicates the weighted mean velocity over the corresponding x-axis region, and the shaded green indicates the 1σ error in the mean. b) SALT finder chart for ESO343-G014 showing the position of the slit in red.

located ~ 450 kpc to the southwest. The background QSO RBS2000 is located northeast at $\rho = 314$ kpc and 64° azimuth angle on the approaching side of IC5325. We detect Ly α at $v_{\text{Ly}\alpha} = 1598$ km s $^{-1}$ ($\Delta v = 86$ km s $^{-1}$) towards RBS2000. While this velocity is anti-aligned with the rotation the disk gas relative to our model predictions (cylindrical = [-41, -20], NFW = [-29, 1] km s $^{-1}$), the low inclination angle of IC5325 leads to a highly uncertain position angle. Without additional observations, we cannot say for certain if the location of RBS2000 actually lies on the approaching or receding side. This position angle uncertainty also means our SALT rotation curve is a lower limit on the true rotation velocity of IC5325.

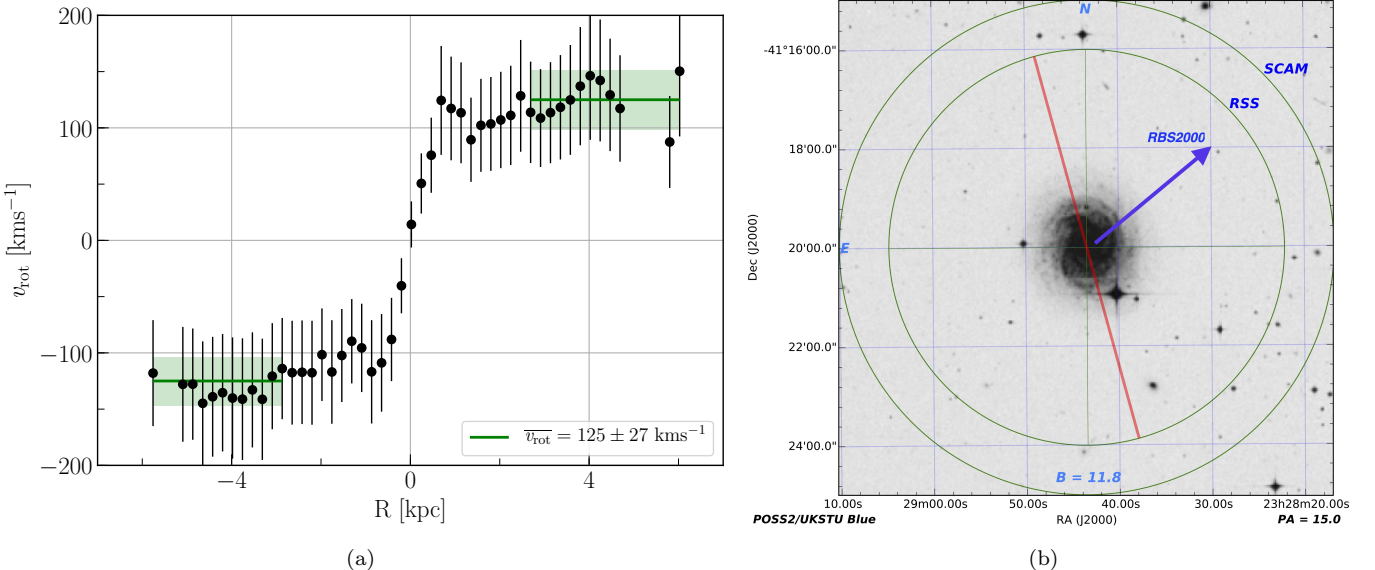


Figure 9. a) Rotation curve of IC5325. The solid green line indicates the weighted mean velocity over the corresponding x-axis region, and the shaded green indicates the 1σ error in the mean. b) SALT finder chart for IC5325 showing the position of the slit in red.

A.4. MCG-03-58-009

MCG-03-58-009 is a massive and very isolated Sc type galaxy at a measured systemic velocity of $v_{\text{sys}} = 9015 \pm 19 \text{ km s}^{-1}$ and inclination angle of $i = 61^\circ$. The background QSO MRC2251-178 is located southeast at $\rho = 355 \text{ kpc}$ at an azimuth angle of 71° on the receding side. We detect a weak Ly α absorber at $v_{\text{Ly}\alpha} = 9029 \text{ km s}^{-1}$ ($\Delta v = 14 \text{ km s}^{-1}$) towards MRC2251-178. This absorber velocity falls well within the expected range for co-rotation relative to our models (cylindrical = [-26, 137], NFW = [-42, 83] km s^{-1}). Although this absorber matches the velocity expected for co-rotation, the velocity difference ($\Delta v = 14 \text{ km s}^{-1}$) is also within the systemic velocity uncertainty for MCG-03-58-009. The relative weakness of this absorber ($\text{EW} = 62 \pm 4 \text{ m}\AA$) is somewhat unusual given it's proximity (just outside of $1 R_{\text{vir}}$) to a massive galaxy. If this is representative of an isolated system such as MCG-03-58-009, then we should expect the halo rotational velocity to approach systemic by $1 R_{\text{vir}}$.

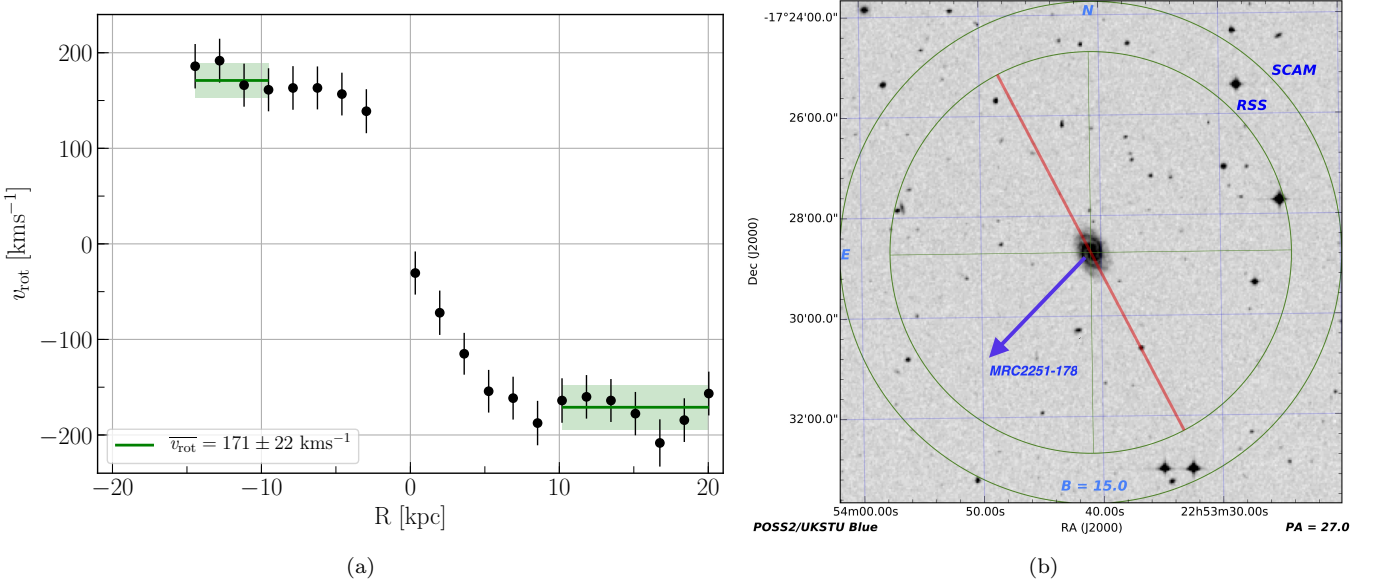


Figure 10. a) Rotation curve of MCG-03-58-009. The solid green line indicates the weighted mean velocity over the corresponding x-axis region, and the shaded green indicates the 1σ error in the mean. b) SALT finder chart for MCG-03-58-009 showing the position of the slit in red.

A.5. NGC1566

NGC1566 is a mostly face-on ($i = 19^\circ$) SAB(rs)bc type galaxy with measured systemic velocity of $v_{\text{sys}} = 1502 \pm 15 \text{ km s}^{-1}$ and inclination angle of $i = 19^\circ$. There are several other large galaxies at $\rho \gtrsim 200 \text{ kpc}$ from NGC1566 (e.g., NGC1549, NGC1596, and NGC1581). The closest QSO sightline is toward HE0429-5343, northeast of NGC1566 at $\rho = 256 \text{ kpc}$ and 60° azimuth angle. We detect Ly α absorption toward HE0429-5343 at $v_{\text{Ly}\alpha} = 1167, 1358 \text{ km s}^{-1}$ ($\Delta v = -335, -144 \text{ km s}^{-1}$). Both of these absorbers have the correct velocity sign, but we would expect a smaller velocity for co-rotation based on our model results (cylindrical = [-53, -2], NFW = [-22, 17] km s^{-1}). Unfortunately NGC1617 is slightly closer to this sightline than NGC1566, at $\rho = 233 \text{ kpc}$ and $v_{\text{sys}} = 1063 \text{ km s}^{-1}$, so it is not possible to confidently attribute these absorbers to NGC1566.

A more distant QSO sightline toward 1H0419-577 is located to the south at $\rho = 303 \text{ kpc}$ and just east of the receding side of the major axis at an azimuth angle of 10° . We detect Ly α at $v_{\text{Ly}\alpha} = 1123, 1188, 1264 \text{ km s}^{-1}$ ($\Delta v = -379, -314, -238 \text{ km s}^{-1}$), all of which are the wrong sign for co-rotation relative to our models (cylindrical = [48, 76], NFW = [-2, 31] km s^{-1}). This sightline is also actually closer to a small group of galaxies including NGC1549, NGC1546 and NGC1536, all with systemic velocities near $\sim 1200 \text{ km s}^{-1}$. Additionally, this absorber system contains C III, C IV, Si II, Si III, Si IV lines. These lines likely are associated with this group rather than with NGC1566.

A.6. NGC3513

NGC3513 a mostly face-on ($i = 30^\circ$) SB(rs)c galaxy with measured systemic velocity $v_{\text{sys}} = 1204 \pm 12 \text{ km s}^{-1}$. It has a companion galaxy in NGC3511 at $\rho = 44 \text{ kpc}$ and $v_{\text{sys}} = 1109 \text{ km s}^{-1}$ (NGC3513 diameter $D = 22.1 \text{ kpc}$, NGC3511 diameter $D = 28.1 \text{ kpc}$). The background QSO H1101-232 is located directly south of the pair at $\rho = 60 \text{ kpc}$ and

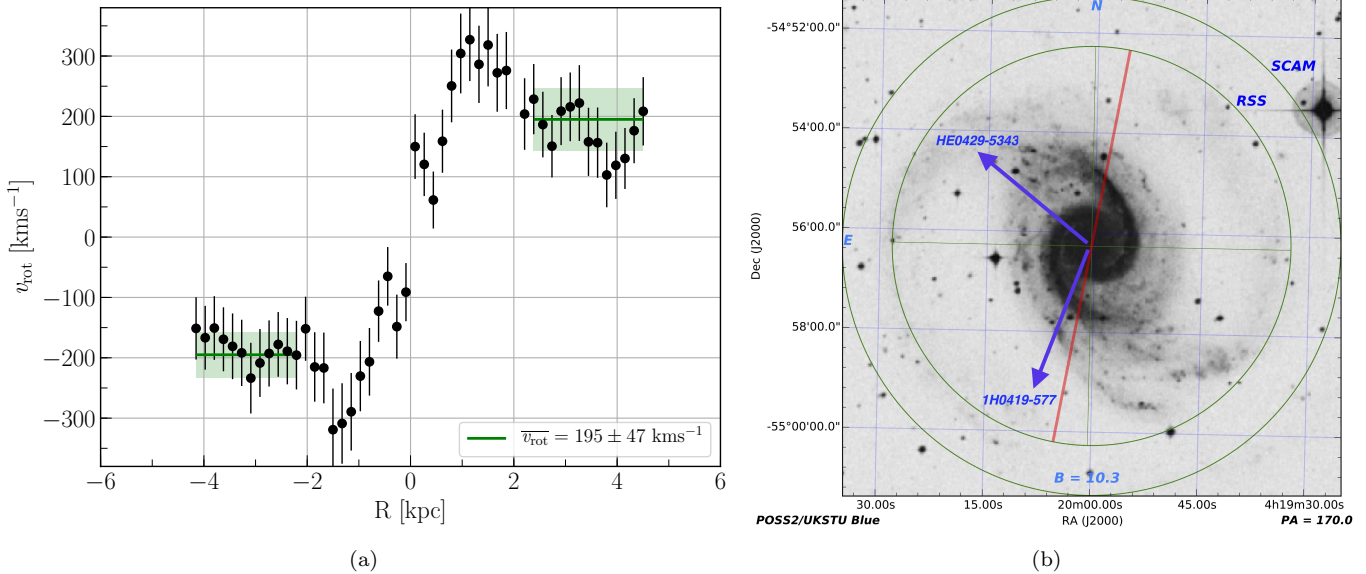


Figure 11. a) Rotation curve of NGC1566. The solid green line indicates the weighted mean velocity over the corresponding x-axis region, and the shaded green indicates the 1σ error in the mean. b) SALT finder chart for NGC1566 showing the position of the slit in red.

azimuth angle of 67° on the receding side. We detect Ly α at $v_{\text{Ly}\alpha} = 1182 \text{ km s}^{-1}$ ($\Delta v = -22 \text{ km s}^{-1}$) toward H1101-232. NGC3513 appears to be rotating slowly, with a maximal inclination-corrected rotation velocity of $v_{\text{rot}} / \sin(i) = 22 \pm 24 \text{ km s}^{-1}$. The $\Delta v = -22 \text{ km s}^{-1}$ for this absorber is opposite in sign for co-rotation on the sky and just outside our predicted model velocity range (cylindrical = [-19, 27], NFW = [-19, 28] km s $^{-1}$). Given that NGC3511 is so close, this absorber's velocity is probably subject to a complex velocity field influenced by both NGC3511 and NGC3513. For this reason we have marked this galaxy as "uncertain" in all map plots and have not included it in our statistical results. This absorber system also contains C IV, N V, Si II, Si III, and Si IV lines.

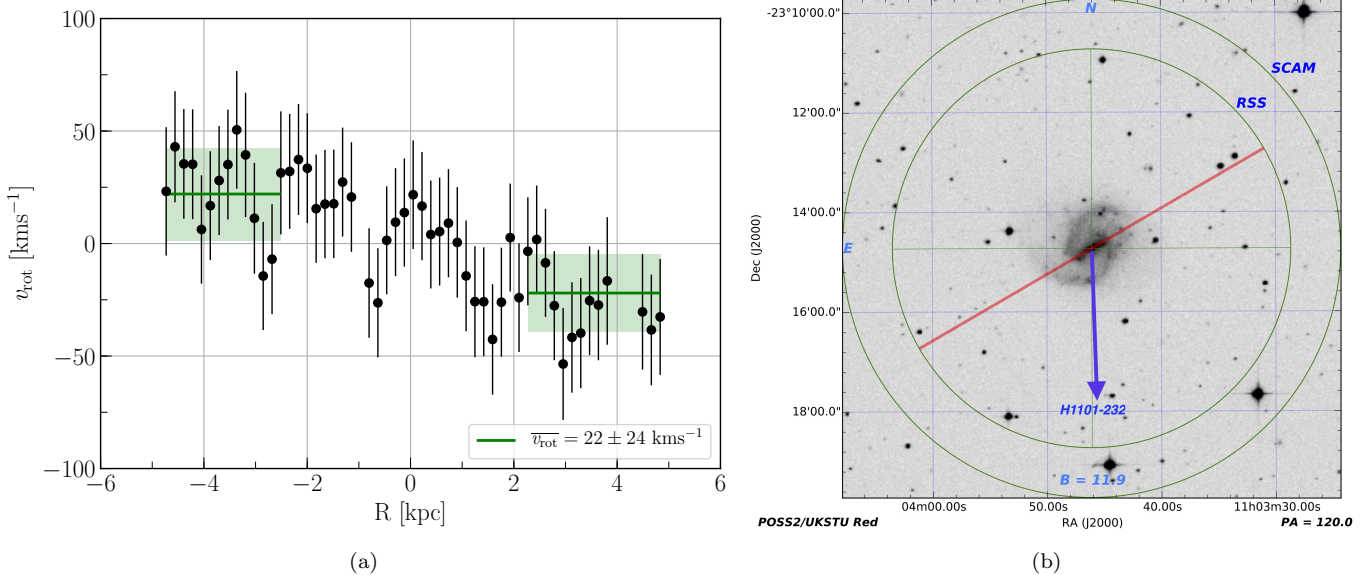


Figure 12. a) Rotation curve of NGC3513. The solid green line indicates the weighted mean velocity over the corresponding x-axis region, and the shaded green indicates the 1σ error in the mean. b) SALT finder chart for NGC3513 showing the position of the slit in red.

A.7. NGC3633

NGC3633 is an isolated, edge-on ($i = 72^\circ$) SAa type galaxy with a measured systemic velocity $v_{\text{sys}} = 2587 \pm 7 \text{ km s}^{-1}$. Several locations along the disk of NGC3633 show two velocities for emission. We have combined these into a single velocity measurement via a weighted average.

The background QSO RX_J1121.2+0326 is located southeast at $\rho = 184$ kpc and 58° azimuth on the approaching side of NGC3633. We detect Ly α at $v_{\text{Ly}\alpha} = 2605 \text{ km s}^{-1}$ ($\Delta v = 18 \text{ km s}^{-1}$) toward RX_J1121.2+0326. While close to v_{sys} , this absorber velocity is just outside our predicted model velocities (cylindrical = [-153, -14], NFW = [-77, 10] km s^{-1}). However, this absorber is also very weak and broad, making the velocity center uncertain by at least $\sim 10 \text{ km s}^{-1}$. Taking this along with the uncertainty in V_{sys} , this absorber could still be consistent with co-rotation.

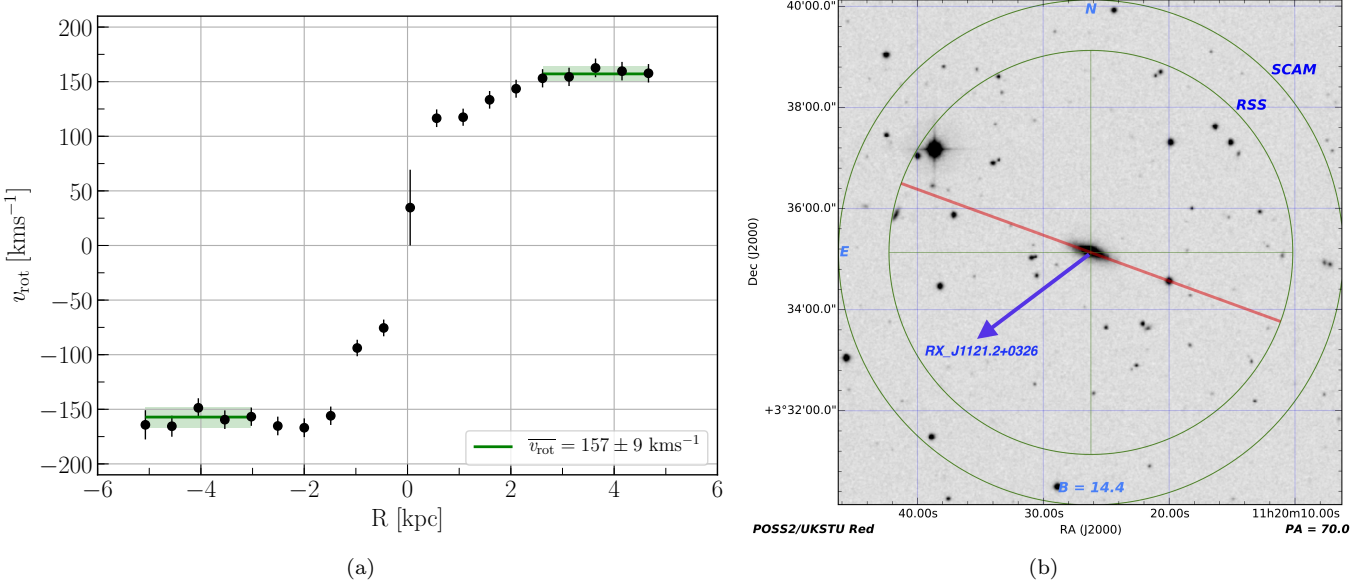


Figure 13. a) Rotation curve of NGC3633. The solid green line indicates the weighted mean velocity over the corresponding x-axis region, and the shaded green indicates the 1σ error in the mean. b) SALT finder chart for NGC3633 showing the position of the slit in red.

A.8. NGC4536

NGC4536 is a SAB(rs)bc type galaxy located in the Virgo Cluster at a measured systemic velocity of $v_{\text{sys}} = 1867 \pm 33 \text{ km s}^{-1}$ and inclination $i = 61^\circ$. The data on the receding side of NGC4536 is messy, and may include contamination from background sources. Hence, our measured systemic velocity, and thus rotation velocity of $139 \pm 37 \text{ km s}^{-1}$, have relatively high uncertainty. Other published redshift values available from NED and rotation velocities from the HyperLEDA database are broadly consistent with our values, albeit biased slightly lower and higher in velocity, respectively.

There are 2 sightlines to the southwest of NGC4536, both on the receding side of the galaxy. HE1228+0131 at $\rho = 338$ kpc and 86° azimuth has 5 Ly α lines: $v_{\text{Ly}\alpha} = 1495, 1571, 1686, 1721, 1854 \text{ km s}^{-1}$ ($\Delta v = -372, -296, -181, -146, -13 \text{ km s}^{-1}$). None of these are of the correct orientation for co-rotation relative to our model predictions (cylindrical = [18, 51], NFW = [2, 32] km s^{-1}), and all are more likely to be associated with other nearby galaxies, such as NGC4517A, which is slightly closer to these absorbers in impact parameter and velocity than is NGC4536. At $v_{\text{Ly}\alpha} = 1686 \text{ km s}^{-1}$ we also detect C II, C IV, Si II, Si III, and Si IV, and at $v_{\text{Ly}\alpha} = 1721 \text{ km s}^{-1}$ we detect Lyman series from Ly α to Ly θ as well as C II, C III, C IV, Si II, Si III, and Si IV.

The second nearby sightline is toward 3C273 at $\rho = 344$ kpc and 46° azimuth angle, and shows 3 Ly α lines at $v_{\text{Ly}\alpha} = 1580, 2156, 2267 \text{ km s}^{-1}$ ($\Delta v = -287, 289, 400 \text{ km s}^{-1}$). Two of these are correctly oriented for co-rotation relative to our model predictions (cylindrical = [87, 121], NFW = [5, 41] km s^{-1}), but are too high in velocity to make this scenario probable. Overall, given the number of nearby galaxies and their locations, we would expect these absorbers to trace the overall velocity field instead of the halo rotation of any particular galaxy. After this galaxy was included in the SALT observing queue we realized it is actually located in the Virgo cluster, so we have decided to remove it from the statistical sample in this paper but present the observed data here nonetheless.

A.9. NGC4939

NGC4939 is a large SA(s)bc type galaxy with measured systemic velocity $v_{\text{sys}} = 3093 \pm 33 \text{ km s}^{-1}$ and inclination $i = 61^\circ$. The background QSO PG1302-102 is located southeast at $\rho = 254$ kpc and 61° azimuth angle on the approaching side of NGC4939. We detect a Ly α absorber at $v_{\text{Ly}\alpha} = 3448 \text{ km s}^{-1}$ ($\Delta v = 355 \text{ km s}^{-1}$) towards PG1302-102. As this absorber is located on the approaching side, we can easily rule out co-rotation in this case. NGC4939 does not have any close neighbors, so represents an intriguing case against co-rotation for gas past $1R_{\text{vir}}$.

A.10. NGC5364

NGC5364 is a SA(rs)bc pec type galaxy at a measured systemic velocity $v_{\text{sys}} = 1238 \pm 17 \text{ km s}^{-1}$ and inclination $i = 57^\circ$. It is located in a group environment with 5 other large, nearby galaxies. The background QSO SDSSJ135726.27+043541.4 is located southeast at $\rho = 165$ kpc and 84° azimuth angle on the receding side of NGC5364. We detect Ly α at $v_{\text{Ly}\alpha} = 967, 1124 \text{ km s}^{-1}$ ($\Delta v = -271, -114 \text{ km s}^{-1}$) toward SDSSJ135726.27+043541.4. These absorbers have the opposite sign for co-rotation relative to our model predictions (cylindrical = [-26, 108], NFW = [-30, 68] km s^{-1}). However, because of the orientation of NGC5364 on the sky with respect to this sightline, these absorbers lie extremely close to the inflection point where projected rotation velocities flip to approaching instead of receding. For example, shifting the location of SDSSJ135726.27+043541.4 east by a tenth of a degree (~ 20 kpc) is sufficient to put these absorbers on the approaching side of NGC5364. Hence, both of these absorbers could be co-rotating with NGC5364 given very reasonable assumptions on the shape of an extended disk. Nonetheless, the fact that this system lives in galaxy group environment likely dominates the surrounding velocity field.

A.11. NGC5786

NGC5786 is a large, strongly-barred spiral galaxy with measured systemic velocity $v_{\text{sys}} = 2975 \pm 22 \text{ km s}^{-1}$ and inclination $i = 65^\circ$. The background QSO QSO1500-4140 is located directly east at $\rho = 453$ kpc and 1° azimuth angle on the receding side of NGC5786. We detect Ly α at $v_{\text{Ly}\alpha} = 3138 \text{ km s}^{-1}$ ($\Delta v = 163 \text{ km s}^{-1}$) toward QSO1500-4140, which is slightly above the model predicted velocity range (cylindrical = [106, 160], NFW = [19, 67] km s^{-1}). However, the two neighboring galaxies ESO327-G038 and ESO327-G039 are both located south of NGC5786 at $\rho = 62, 296$ kpc, respectively. These nearby galaxies, along with the large distance to the absorption ($\sim 2.5R_{\text{vir}}$), make it difficult to believe there is a connection to a NGC5786 extended disk.

A.12. UGC09760

UGC09760 is an edge-on ($i = 90^\circ$), slow-rotating Sd galaxy with measured systemic velocity $v_{\text{sys}} = 2094 \pm 16 \text{ km s}^{-1}$. This systemic velocity deviates slightly from other published redshifts, such as the The Updated Zwicky Catalog value

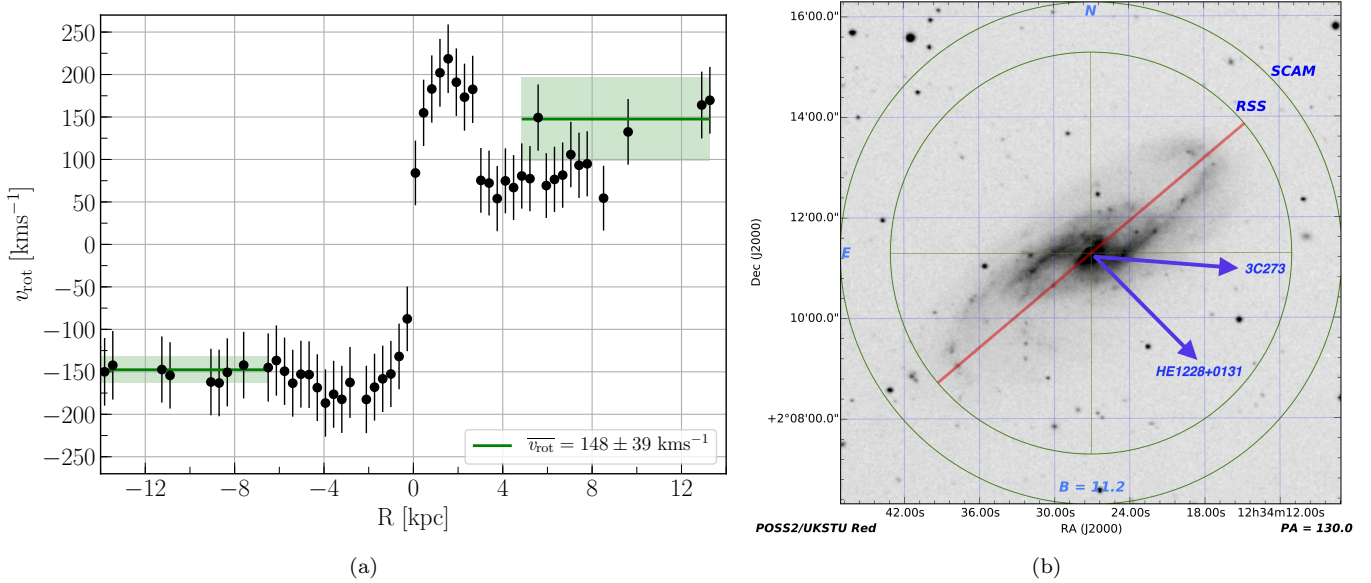


Figure 14. a) Rotation curve of NGC4536. The solid green line indicates the weighted mean velocity over the corresponding x-axis region, and the shaded green indicates the 1σ error in the mean. b) SALT finder chart for NGC4536 showing the position of the slit in red.

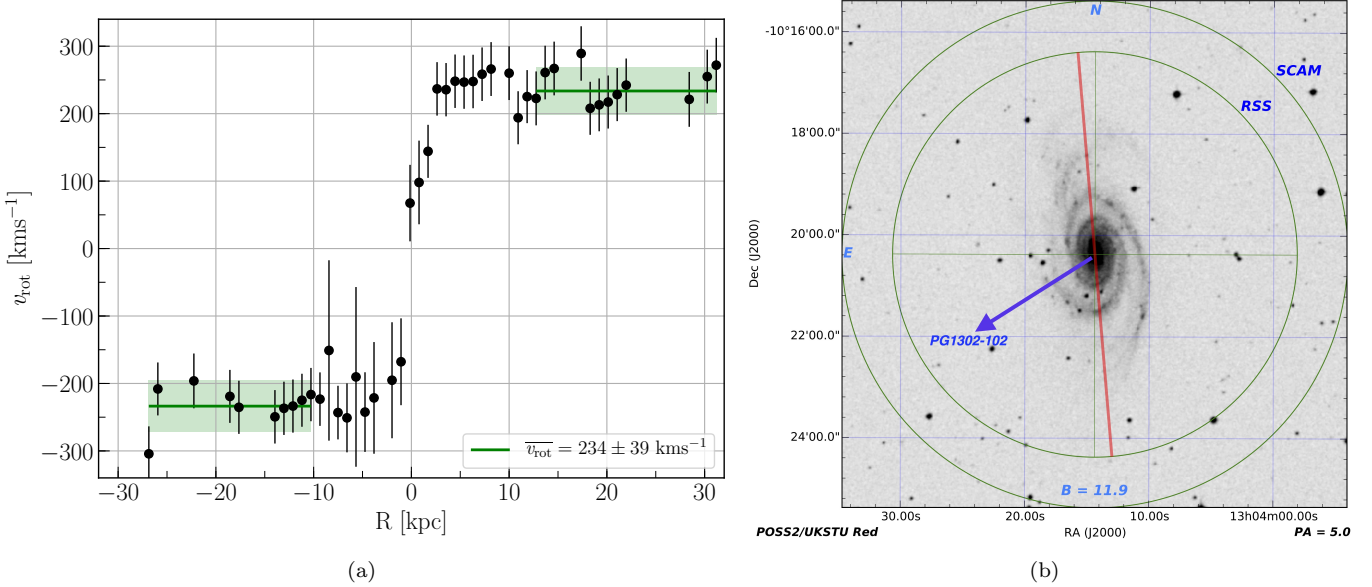


Figure 15. a) Rotation curve of NGC4939. The solid green line indicates the weighted mean velocity over the corresponding x-axis region, and the shaded green indicates the 1σ error in the mean. b) SALT finder chart for NGC4939 showing the position of the slit in red.

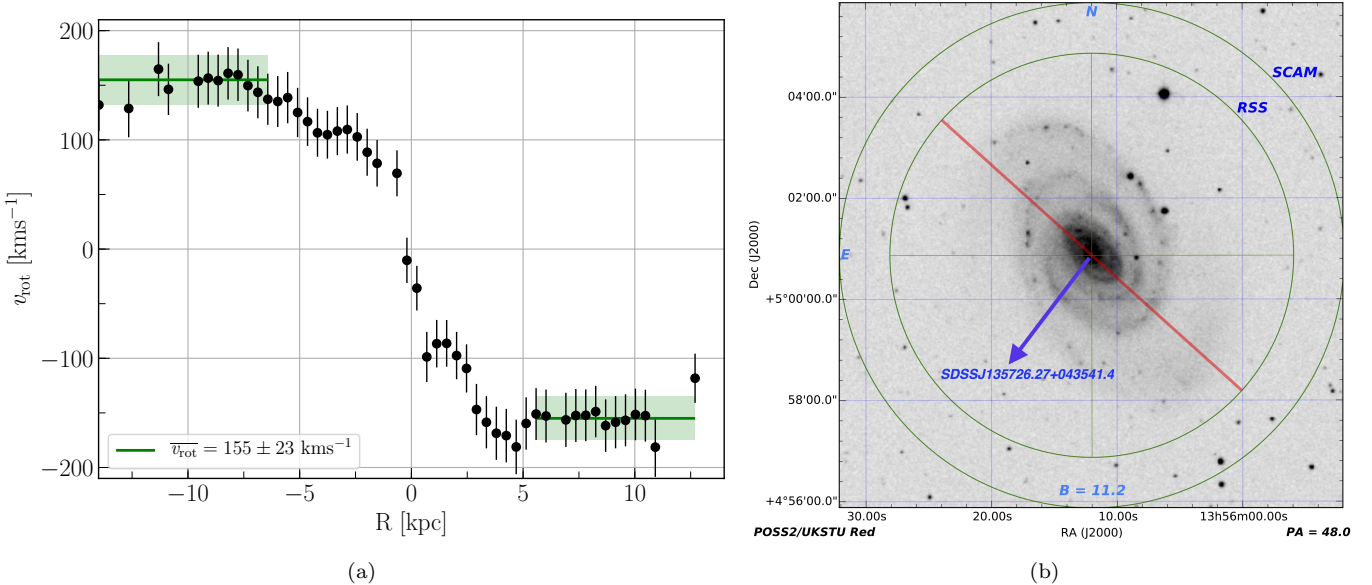


Figure 16. a) Rotation curve of NGC5364. The solid green line indicates the weighted mean velocity over the corresponding x-axis region, and the shaded green indicates the 1σ error in the mean. b) SALT finder chart for NGC5364 showing the position of the slit in red.

of $v_{\text{sys}} = 2023 \pm 2 \text{ km s}^{-1}$ (Falco et al. 1999). This is likely due to our method of imposing rotation symmetry and averaging the approaching and receding velocities to derive v_{sys} . If we do not sample the rotation curve far enough out, a systematic offset is not unreasonable. Indeed, we do not detect the rotation curve turnover or flattening point.

The background QSO SDSSJ151237.15+012846.0 is located southeast at $\rho = 123$ kpc and 90° azimuth angle. We detect Ly α absorption at $v_{\text{Ly}\alpha} = 2029 \text{ km s}^{-1}$ ($\Delta v = -65 \text{ km s}^{-1}$) toward SDSSJ151237.15+012846.0. This velocity falls outside the model predictions for co-rotation (cylindrical = [-30, 30], NFW = [-30, 86] km s $^{-1}$), but unfortunately this sightline lies almost exactly at an azimuth of 90° . Hence, the motion of this gas could easily be either co-rotating or counter-rotating depending on a minute change in the position angle assigned to UGC09760. This is especially true

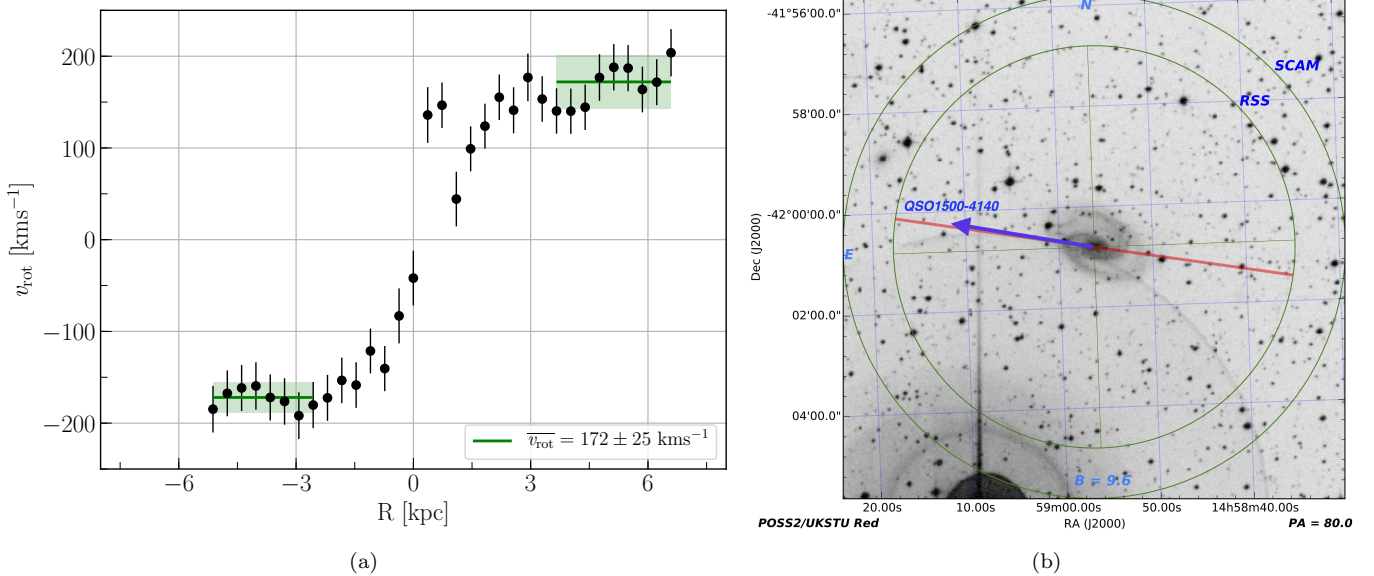


Figure 17. a) Rotation curve of NGC5786. The solid green line indicates the weighted mean velocity over the corresponding x-axis region, and the shaded green indicates the 1σ error in the mean. b) SALT finder chart for NGC5786 showing the position of the slit in red.

if we assume our measured v_{sys} is erroneously high, and indeed closer to the values obtained by other observations. For example, if we adjust the position angle by a single degree, to 56° instead of 57° , our model predictions become (cylindrical = [-30, 30], NFW = [-79, 30] km s $^{-1}$) and this absorber becomes consistent with co-rotation in the NFW model.

It is worth noting that there are several small satellite galaxies nearby, including SDSSJ151208.16+013508.5, SDSSJ151121.63+013637.6, SDSSJ151241.38+013723.7 and UGC09746 (impact parameters $\rho = 53, 88, 82, 230$ kpc respectively). All of these galaxies lie slightly blue-ward of UGC09760, and thus *further* away in velocity from the Ly α absorber at 2029 km s $^{-1}$.

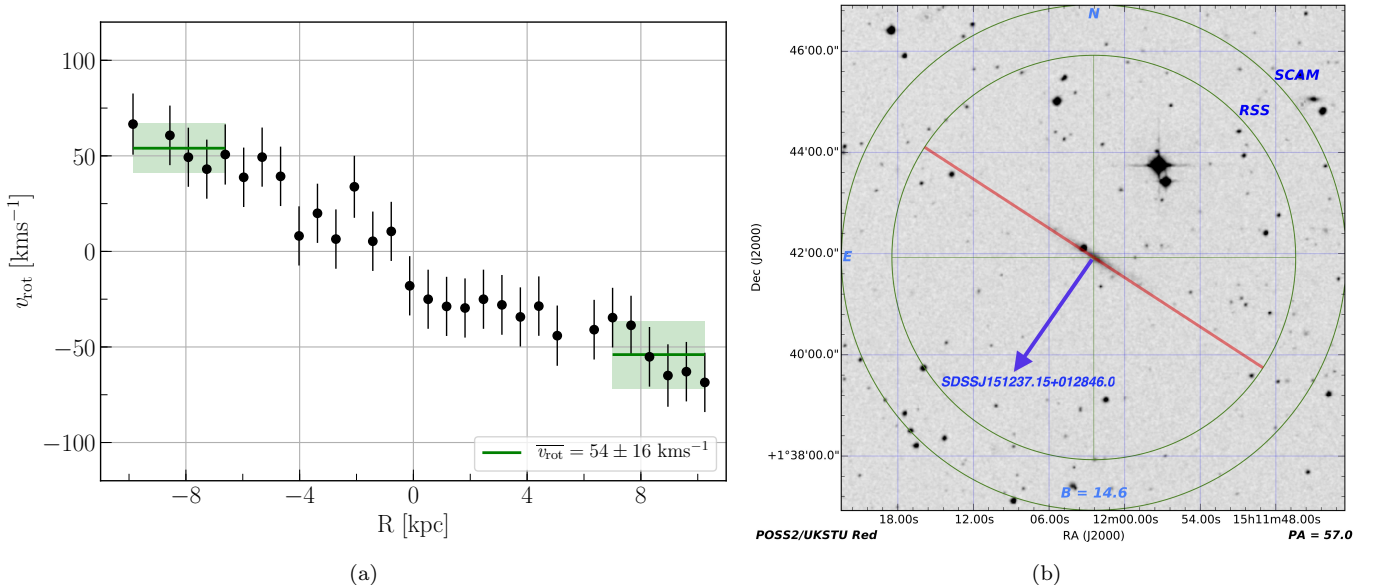


Figure 18. a) Rotation curve of UGC09760. The solid green line indicates the weighted mean velocity over the corresponding x-axis region, and the shaded green indicates the 1σ error in the mean. b) SALT finder chart for UGC09760 showing the position of the slit in red.

B. ANCILLARY DATA

To increase our sample size we have also searched the literature for galaxies with published rotation curves and orientations. Unfortunately, while the rotation velocity is available for thousands of galaxies, only a handful of publications also include the *orientation* of the rotation on the sky. Of these, we were able to find 18 additional galaxies which have a systemic velocity greater than $\sim 500 \text{ km s}^{-1}$, and are near to a COS or STIS sightline with available data. We have included 3 of the galaxy-QSO systems analyzed by Côté et al. (2005). We briefly summarize each of these systems here (see Sections B.14 - B.9), and refer the reader to Côté et al. (2005) for a more complete discussion. As new spectra and redshift-independent distances are available for these systems our results, while similar, are not identical.

B.1. NGC2770

NGC2770 is a large, edge-on ($i = 80^\circ$) Sc type galaxy with systemic velocity $v_{\text{sys}} = 1948 \pm 2 \text{ km s}^{-1}$. It is mostly isolated except for two nearby small dwarfs MCG+06-20-036NED02 and GALEXASCIJ090946.88+330840.4 (both 25 kpc away, on opposite sides of NGC2770). We take the rotation curve and orientation information produced by Rhee & van Albada (1996). There are five nearby QSOs, which we present in order of increasing impact parameter.

First, the QSO FBQSJ0908+3246 is located south at $\rho = 204$ kpc and 59° azimuth angle on the approaching side of NGC2770. We detect Ly α at $v_{\text{Ly}\alpha} = 1915, 1982 \text{ km s}^{-1}$ ($\Delta v = -33, 34 \text{ km s}^{-1}$). Relative to our model predictions (cylindrical = [-146, -4], NFW = [-117, 10] km s^{-1}), only the lower velocity line can be described as co-rotating.

Second, the QSO TON1015 is located northeast at $\rho = 218$ kpc and 61° azimuth angle on the receding side of NGC2770. We detect Ly α at $v_{\text{Ly}\alpha} = 1833, 1985 \text{ km s}^{-1}$ ($\Delta v = -115, 37 \text{ km s}^{-1}$). Relative to our model predictions (cylindrical = [3, 146], NFW = [-10, 115] km s^{-1}), only the higher velocity absorber can be described as co-rotating.

Third the QSO SDSSJ091127.30+325337.0 is located southeast at $\rho = 234$ kpc and 30° azimuth angle on the approaching side of NGC2770. We detect Ly α at $v_{\text{Ly}\alpha} = 2063 \text{ km s}^{-1}$ ($\Delta v = 115 \text{ km s}^{-1}$). Relative to our model predictions (cylindrical = [-150, -43], NFW = [-117, -19] km s^{-1}), this absorber appears to be counter-rotating.

Fourth, the QSO SDSSJ091052.80+333008.0 is located northeast at $\rho = 239$ kpc and 66° azimuth angle on the receding side of NGC2770. We detect Ly α at $v_{\text{sys}} = 1824, 1975 \text{ km s}^{-1}$ ($\Delta v = -124, 27 \text{ km s}^{-1}$). Relative to our model predictions (cylindrical = [6, 145], NFW = [-7, 112] km s^{-1}), only the higher velocity absorber can be described as co-rotating.

Finally, the QSO TON1009 is located south at $\rho = 267$ kpc and 41° azimuth angle on the approaching side of NGC2770. We detect Ly α at $v_{\text{sys}} = 1908, 1980 \text{ km s}^{-1}$ ($\Delta v = -40, 32 \text{ km s}^{-1}$). Relative to our model predictions (cylindrical = [-146, -39], NFW = [-110, -14] km s^{-1}), only the lower velocity absorber can be described as co-rotating.

Interestingly, we appear to be detecting extended gas structures in these 5 sightlines. Toward the northeast we find TON1015 and SDSSJ091052.80+333008.0 and a set of absorber pairs at $v_{\text{Ly}\alpha} = 1833, 1824 \text{ km s}^{-1}$ and $v_{\text{Ly}\alpha} = 1985, 1975 \text{ km s}^{-1}$ each having very similar EW and $N_{\text{H I}}$, and remarkably similar appearing line-structure. Adopting a distance of 28.6 Mpc to this cloud, we calculate a linear separation between TON1015 and SDSSJ091052.80+333008.0 of 28 kpc. Hence, there appears to be two distinct clouds of at least 28 kpc in physical extent sandwiched around the systemic velocity of NGC2770. Toward the south we find TON1009 and FBQ SJ0908+3246 and a set of absorber pairs at $v_{\text{Ly}\alpha} = 1908, 1915 \text{ km s}^{-1}$ and $v_{\text{Ly}\alpha} = 1980, 1982 \text{ km s}^{-1}$, again with similar EW, $N_{\text{H I}}$ and line-shapes.

B.2. NGC3067

NGC3067 is a mostly edge-on ($i = 71^\circ$) SAB(s)ab type galaxy with systemic velocity $v_{\text{sys}} = 1465 \pm 5 \text{ km s}^{-1}$. This galaxy and the nearby QSO sightline toward 3C232 is a particularly well studied system. They are separated by only $\rho = 11$ kpc (74° azimuth angle on the northwest, receding side) and a Lyman Limit System (LLS) with column density $N_{\text{H I}} = 1 \times 10^{20} \text{ cm}^{-2}$ is detected toward 3C232 at $v_{\text{Ly}\alpha} = 1408 \text{ km s}^{-1}$, which has been postulated as a high velocity cloud (HVC) orbiting NGC3067 (Carilli et al. 1989; Keeney et al. 2005).

We obtained the rotation curve for NGC3067 from Rubin et al. (1982) and the orientation from Carilli et al. (1989). While H I measurements of this LLS fit a single component (at $v_{\text{H I}} = 1421 \text{ km s}^{-1}$), we have fit 3 separate components at $v_{\text{Ly}\alpha} = 1408, 1510, 1641 \text{ km s}^{-1}$ ($\Delta v = -57, 45, 176 \text{ km s}^{-1}$) to match the associated metal lines (namely, C IV, Si II, Si III, Si IV, Mg II, Fe II, and N I all show at least 2 separate components). This splitting has been analyzed in detail most recently by Keeney et al. (2005) and Stocke et al. (2010), who find similar but slightly lower $v_{\text{Ly}\alpha}$ for all three absorbers. Only the lowest velocity component can strictly be described by our model velocity range (cylindrical = [-121, 25], NFW = [-139, 26] km s^{-1}), however the $v_{\text{Ly}\alpha} = 1510 \text{ km s}^{-1}$ component is also very close to this range. The $v_{\text{Ly}\alpha} = 1641 \text{ km s}^{-1}$ component, however, must be either a counter-rotating clouddlet or an outflow directed away from our line of sight.

A second QSO SDSSJ095914.80+320357.0 is located farther away, to the southeast at $\rho = 128$ kpc and 43° azimuth angle on the receding side of NGC3067. We detect Ly α at $v_{\text{Ly}\alpha} = 1493 \text{ km s}^{-1}$ ($\Delta v = 28 \text{ km s}^{-1}$), which agrees well with our model predicted velocity range (cylindrical = [11, 138], NFW = [-12, 81] km s^{-1}).

B.3. NGC3198

NGC3198 is a SB(rs)c type galaxy with systemic velocity $v_{\text{sys}} = 660 \pm 1 \text{ km s}^{-1}$ and inclination $i = 73^\circ$. It is a well studied galaxy, and is included in the detailed THINGS rotation curve study of de Blok et al. (2008). We extracted the raw rotation curve derived by de Blok et al. (2008) using the plot digitization software WebPlotDigitizer⁴. NGC3198 has an even and flat rotation curve, with an average velocity of $v_{\text{rot}} = 152 \text{ km s}^{-1}$. The background QSO RX_1017.5+4702 is located northeast at $\rho = 370 \text{ kpc}$ and 55° azimuth angle on the approaching side of NGC3198. We detect Ly α toward RX_1017.5+4702 at $v_{\text{Ly}\alpha} = 629 \text{ km s}^{-1}$ ($\Delta v = -32 \text{ km s}^{-1}$), which can nicely be described by a co-rotating disk based on our model predicted velocity range (cylindrical = [-153, -21], NFW = [-91, 6] km s^{-1}). We note that the small dwarf galaxy SDSSJ101848.77+452137.0 is located 65 kpc away from NGC3198 toward the southwest.

B.4. NGC3351

NGC3351 is a mostly face-on ($i = 42^\circ$) SB(r)b type galaxy with systemic velocity $v_{\text{sys}} = 778 \pm 4 \text{ km s}^{-1}$. It is located $\sim 200 \text{ kpc}$ southwest of the core of the Leo I group. We take the rotation curve and orientation produced by Dicaine et al. (2008). While we expect any extended disk rotation to be quickly disrupted due to the complex Leo I environment, this galaxy also has one of the closest sightlines in our sample with SDSSJ104335.90+115129.0 at $\rho = 31 \text{ kpc}$ and 13° azimuth on the northwest, approaching side. We detect Ly α at $v_{\text{Ly}\alpha} = 717, 882, 1030 \text{ km s}^{-1}$ ($\Delta v = -61, 104, 252 \text{ km s}^{-1}$) toward this sightline. The lowest velocity absorber agrees nicely with both models for co-rotation, while the other two are above our model predictions (cylindrical = [-99, 12], NFW = [-68, 20] km s^{-1}). We also detect multiple metal ions associated with the $v_{\text{Ly}\alpha} = 717 \text{ km s}^{-1}$ line, including C II, N I, N V, O I, Si II, Si III, Si IV, S II, and Fe II.

B.5. NGC3432

NGC3432 is an edge-on ($i = 90^\circ$) SB(s)m type galaxy with systemic velocity $v_{\text{sys}} = 616 \pm 4 \text{ km s}^{-1}$. It is interacting with the nearby dwarf galaxy UGC05983 located 11 kpc away and at $v_{\text{sys}} = 765 \text{ km s}^{-1}$. We take a rotation curve and orientation for NGC3432 from Rhee & van Albada (1996). The QSO CSO295 is located just 20 kpc away and just to the receding side of the minor axis (82° azimuth angle). This is the second closest pair in our sample, after the 11 kpc separated NGC3067-3C232 system. We detect Ly α at $v_{\text{Ly}\alpha} = 600, 662 \text{ km s}^{-1}$ ($\Delta v = -16, 46 \text{ km s}^{-1}$) toward CSO295. Relative to our model predictions (cylindrical = [-37, 48], NFW = [-37, 134] km s^{-1}) both of these absorbers are consistent with co-rotation. In fact, this orientation would represent the lower-velocity cloud existing toward the near-edge of the halo and the higher velocity cloud lying very close to the plane of the stellar disk. We also detect C II, Si II, Si III, and Si IV associated with this absorption system.

A second QSO RX_J1054.2+3511 is located south at $\rho = 290 \text{ kpc}$ and 57° azimuth angle on the receding side of NGC3432. We detect Ly α at $v_{\text{sys}} = 703 \text{ km s}^{-1}$ ($\Delta v = 87 \text{ km s}^{-1}$) toward RX_J1054.2+3511. Relative to our model predictions (cylindrical = [0, 123], NFW = [-9, 111] km s^{-1}), this absorber is consistent with co-rotation as well.

B.6. NGC3631

NGC3631 is a mostly face-on ($i = 17^\circ$) SA(s)c type galaxy with systemic velocity $v_{\text{sys}} = 1156 \pm 1 \text{ km s}^{-1}$. We take the rotation curve and orientation information produced by Knapen (1997). There are 4 nearby QSOs, which we will present in order of increasing impact parameter.

First, the closest background QSO RX_J1117.6+5301 is located southwest at $\rho = 78 \text{ kpc}$ and 75° azimuth angle on the receding side of NGC3631. We detect Ly α at $v_{\text{Ly}\alpha} = 1131, 1259 \text{ km s}^{-1}$ ($\Delta v = -25, 103 \text{ km s}^{-1}$). Both of these lines fall outside of our model predicted velocities (cylindrical = [10, 24], NFW = [1, 21] km s^{-1}).

Second, background QSO SDSSJ112448.30+531818.0 is located northeast at $\rho = 86 \text{ kpc}$ and 74° azimuth angle on the approaching side of NGC3631. We detect Ly α at $v_{\text{Ly}\alpha} = 1019, 1141 \text{ km s}^{-1}$ ($\Delta v = -137, -15 \text{ km s}^{-1}$). Only the higher velocity absorber falls within our model predicted velocity range (cylindrical = [-26, -11], NFW = [-22, 1] km s^{-1}).

Third, the background QSO SDSSJ111443.70+525834.0 is located in the same direction but farther than RX_J1117.6+5301, at $\rho = 145 \text{ kpc}$ and 72° azimuth angle on the receding side of NGC3631. We detect Ly α at $v_{\text{Ly}\alpha} = 1163 \text{ km s}^{-1}$ ($\Delta v = 7 \text{ km s}^{-1}$). This absorber appears to agree well with our model predicted velocity range (cylindrical = [8, 29], NFW = [-5, 24] km s^{-1}).

Finally, the background QSO SBS1116+523 is located south at $\rho = 163 \text{ kpc}$ and 40° azimuth angle on the approaching side of NGC3631, but we do not detect any Ly α within ± 400 of NGC3631.

B.7. NGC3666

NGC3666 is a mostly isolated and edge-on ($i = 78^\circ$) SA(rs)c type galaxy with systemic velocity $v_{\text{sys}} = 1060 \pm 1 \text{ km s}^{-1}$. We take the rotation curve and orientation information produced by Rhee & van Albada (1996). The QSO

⁴ WebPlotDigitizer; <http://arohatgi.info/WebPlotDigitizer>

SDSSJ112439.50+113117.0 is located north at $\rho = 58$ kpc and 83° azimuth angle on the approaching side of NGC3666. We detect Ly α at $v_{\text{sys}} = 1047, 1099 \text{ km s}^{-1}$ ($\Delta v = -13, 39 \text{ km s}^{-1}$) toward SDSSJ112439.50+113117.0. Relative to our model predictions (cylindrical = [-87, 20], NFW = [-136, 20] km s^{-1}) the lower velocity absorber is consistent with co-rotation, while the other is slightly too high in velocity.

B.8. NGC3726

NGC3726 is a SAB(r)c type galaxy with systemic velocity $v_{\text{sys}} = 866 \pm 1 \text{ km s}^{-1}$ and inclination $i = 53^\circ$ on the southwestern edge of the Ursa Major galaxy cluster (Verheijen & Sancisi 2001). The closest background QSO, CSO1208, is located southeast at $\rho = 369$ kpc and 88° azimuth angle on the receding side of NGC3726. We detect Ly α at $v_{\text{Ly}\alpha} = 731, 874 \text{ km s}^{-1}$ ($\Delta v = -135, 8 \text{ km s}^{-1}$) toward CSO1208. Only the higher velocity absorber falls within our predicted velocity range (cylindrical = [-27, 29], NFW = [-28, 21] km s^{-1}). A more distant QSO, RX_J1142.7+4625, is located in the same direction as CSO1208 at $\rho = 440$ kpc and 86° azimuth angle on the approaching side of NGC3726. We detect Ly α at $v_{\text{Ly}\alpha} = 818 \text{ km s}^{-1}$ ($\Delta v = -48 \text{ km s}^{-1}$), which falls just outside our predicted velocity range (cylindrical = [-34, -14], NFW = [-30, -7] km s^{-1}).

These two QSOs lie very close to and on opposing sides of the minor axis, such that CSO1208 samples the receding side and RX_J1142.7+4625 the approaching. Unfortunately, both are also closer to a small group of dwarf galaxies, including NGC3782 and MCG+08-21-092, $\sim 100 \text{ km s}^{-1}$ blueward of NGC3726. The $v_{\text{sys}} = 731 \text{ km s}^{-1}$ line toward CSO1208 is likely associated with this dwarf group, and the other lines may also be.

B.9. UGC04238

UGC04238 is an isolated, mostly edge-on ($i = 62^\circ$) SBd type galaxy with systemic velocity $v_{\text{sys}} = 1544 \pm 7 \text{ km s}^{-1}$. We take the rotation curve and orientation information produced by Côté et al. (2005). The background QSO PG0804+761 is located directly south at $\rho = 148$ kpc and 59° azimuth on the receding side of UGC04238. We detect Ly α at $v_{\text{Ly}\alpha} = 1526, 1593 \text{ km s}^{-1}$ ($\Delta v = -18, 49 \text{ km s}^{-1}$) toward PG0804+761. Relative to our model predictions (cylindrical = [-3, 86], NFW = [-10, 75] km s^{-1}), although both are close, only the absorber at 1593 km s^{-1} (the lower EW of the two) falls within the expected velocity range for co-rotation.

B.10. NGC4529

NGC4529 is an edge-on ($i = 80^\circ$) and isolated Scd type galaxy with systemic velocity $v_{\text{sys}} = 2536 \pm 11 \text{ km s}^{-1}$. We take the rotation curve and orientation information produced by Côté et al. (2005). The QSO MRK771 is located west at $\rho = 159$ kpc and 23° azimuth angle on the approaching side of NGC4529. We detect Ly α at $v_{\text{sys}} = 2553 \text{ km s}^{-1}$ ($\Delta v = 17 \text{ km s}^{-1}$), which is anti-rotating relative to our model predictions (cylindrical = [-103, -40], NFW = [-87, -25] km s^{-1}). As Côté et al. (2005) conclude, “there is simply no physical way to produce such a velocity with an extending co-rotating disk.”

B.11. NGC4565

NGC4565 is an edge-on ($i = 86^\circ$) SA(s)b type galaxy with systemic velocity $v_{\text{sys}} = 1230 \pm 5 \text{ km s}^{-1}$. We take the rotation curve and orientation produced by Sofue (1996). The background QSO RX_J1236.0+2641 is located directly north at $\rho = 147$ kpc and 41° azimuth angle on receding side of NGC4565. We detect Ly α absorption at $v_{\text{Ly}\alpha} = 1009, 1166, 1254 \text{ km s}^{-1}$ ($\Delta v = -221, -64, 24 \text{ km s}^{-1}$) toward RX_J1236.0+2641. Only the $v_{\text{Ly}\alpha} = 1254 \text{ km s}^{-1}$ line is consistent with co-rotating gas relative to our model predictions (cylindrical = [-2, 246], NFW = [-30, 144] km s^{-1}). However, the presence of several other nearby galaxies (e.g., NGC4559, NGC4562) surely disrupts any possible extended disk rotation that would otherwise be detectable via sightline absorption.

B.12. NGC5907

NGC5907 is a large, edge-on ($i = 90^\circ$) SA(s)c type galaxy with systemic velocity $v_{\text{sys}} = 667 \pm 3 \text{ km s}^{-1}$. We take the rotation curve and orientation produced by Yim et al. (2014). The background QSO SBS1503+570 is located northwest at $\rho = 413$ kpc and 47° azimuth angle on the receding side of NGC5907. We detect Ly α at $v_{\text{Ly}\alpha} = 708 \text{ km s}^{-1}$ ($\Delta v = 38 \text{ km s}^{-1}$), which falls within the model predictions for co-rotation (cylindrical = [31, 228], NFW = [-24, 101] km s^{-1}). Unfortunately there are several other nearby galaxies, the largest of which being NGC5866 (diameter $D = 20.8$ and impact parameter $\rho = 208$ kpc, versus for NGC5907 - $D = 50.6$ and $\rho = 413$ kpc). Hence, it is difficult to assign this absorber to NGC5907 alone.

B.13. NGC5951

NGC5951 is a large, edge-on ($i = 74^\circ$) SBc type galaxy with systemic velocity $v_{\text{sys}} = 1780 \pm 1 \text{ km s}^{-1}$. We take the rotation curve and orientation for NGC5951 from Rhee & van Albada (1996). The QSO 2E1530+1511 is located

east at $\rho = 55$ kpc and 85° azimuth angle on the receding side of NGC5951. We detect Ly α at $v_{\text{Ly}\alpha} = 1795, 1953 \text{ km s}^{-1}$ ($\Delta v = 15, 173 \text{ km s}^{-1}$) toward 2E1530+1511. Relative to our model predictions (cylindrical = [-31, 114], NFW = [-32, 125] km s^{-1}), the lower velocity absorber is consistent with co-rotation while the other is a bit outside of the upper range. The pair of galaxies NGC5954 and NGC5953 are nearby (~ 100 kpc), but the sightline toward 2E1530+1511 is closer and on the opposite side of NGC5951. Given the systemic velocity for the nearby galaxies NGC5954 and NGC5953 ($v_{\text{sys}} = 1959, 1965 \text{ km s}^{-1}$), this absorber is likely also linked with that system.

B.14. NGC6140

NGC6140 is a small SB(s)cd type galaxy with systemic velocity $v_{\text{sys}} = 910 \pm 4 \text{ km s}^{-1}$ and inclination $i = 49^\circ$. We take the rotation curve and orientation information produced by Côté et al. (2005). A background QSO Mrk876 is located northwest at $\rho = 113$ kpc and azimuth angle 21° (although this is somewhat uncertain; the position angle for NGC6140 could be closer to 60° than our adopted value of 94° due to it being mostly face on, faint, and strongly barred). We detect Ly α at $v_{\text{Ly}\alpha} = 939 \text{ km s}^{-1}$ ($\Delta v = 29 \text{ km s}^{-1}$) toward MRK876. This absorber velocity is of the correct *sign*, but just under the the model predicted velocity range (cylindrical = [40, 101], NFW = [35, 102] km s^{-1}) for co-rotation. However, this absorber is still likely co-rotating given both the velocity and position angle uncertainties. Additionally, we detect Ly β and O VI associated with this Ly α absorber (see Narayanan et al. (2010)).

B.15. UGC06446

UGC06446 is a Sd type galaxy with systemic velocity $v_{\text{sys}} = 645 \pm 1 \text{ km s}^{-1}$ and inclination $i = 52^\circ$ on the far northwest edge of the Ursa Major cluster of galaxies. We take the rotation curve and orientation information produced by Verheijen & Sancisi (2001) and Swaters et al. (2009). The background QSO SDSSJ112448.30+531818.0 is located southwest at $\rho = 143$ kpc and 22° azimuth angle on the receding side of UGC06446. We detect Ly α at $v_{\text{Ly}\alpha} = 664, 1019 \text{ km s}^{-1}$ ($\Delta v = 20, 375 \text{ km s}^{-1}$). The absorber at $v_{\text{Ly}\alpha} = 664$ falls well within our model predicted co-rotation range (cylindrical = [-9, 65], NFW = [-15, 61] km s^{-1}), but the absorber at $v_{\text{Ly}\alpha} = 1019$ is far more likely to be associated with NGC3631 ($\rho = 86$ kpc, $v_{\text{sys}} = 1156 \text{ km s}^{-1}$). We therefore treat these as separate systems.

B.16. NGC7817

NGC7817 is an edge-on ($i = 80^\circ$) SAbc type galaxy with systemic velocity $v_{\text{sys}} = 2309 \pm 4 \text{ km s}^{-1}$. We take the rotation curve and orientation information produced by Rhee & van Albada (1996). The background QSO MRK335 is located southeast at $\rho = 343$ kpc and almost directly along the minor axis of NGC7817 (90° azimuth angle). We detect Ly α at $v_{\text{sys}} = 1954, 2274 \text{ km s}^{-1}$ ($\Delta v = -355, -35 \text{ km s}^{-1}$) toward MRK335. Because these absorbers lie almost exactly along the minor axis, our model predicts a very narrow velocity range for co-rotation (cylindrical = [-26, -24], NFW = [-26, -24] km s^{-1}). While the higher velocity line falls a mere 9 km s^{-1} outside this predicted range, the absorption at 1954 km s^{-1} is likely not directly associated with NGC7817 given the large velocity difference. Additionally, the neighboring dwarf galaxy ESDOF538-02 ($v_{\text{sys}} = 2175 \text{ km s}^{-1}$) appears in the same direction as MRK335 and only $\rho = 57$ kpc away from NGC7817, and NSA126180 ($v_{\text{sys}} = 1950 \text{ km s}^{-1}$) appears only $\rho = 83$ kpc away from MRK335.

B.17. UGC08146

UGC08146 is an isolated and edge-on ($i = 78^\circ$) Sd type galaxy with systemic velocity $v_{\text{sys}} = 670 \pm 1 \text{ km s}^{-1}$. This galaxy (and the nearby QSO PG1259+593) are included in the Côté et al. (2005) sample also, but we have taken the rotation curve and orientation information from Rhee & van Albada (1996). The QSO PG1259+593 is located northwest at $\rho = 114$ kpc at 50° azimuth angle on the receding side of UGC08146. While Côté et al. (2005) cite a single Ly α component at $v_{\text{Ly}\alpha} = 679 \text{ km s}^{-1}$, we detect two components at $v_{\text{Ly}\alpha} = 646, 683 \text{ km s}^{-1}$ ($\Delta v = -24, 13 \text{ km s}^{-1}$), in the higher signal-to-noise COS data now available for PG1259+593. Relative to our model predictions (cylindrical = [-13, 82], NFW = [-16, 83] km s^{-1}), the higher velocity component is consistent with co-rotation, and the other component is only 8 km s^{-1} shy of falling into the NFW co-rotation range as well.